RESEARCH ARTICLE

Key Points:
- Choice of river segmentation strategies affect the quality of reach-averaged products produced by remote sensing
- Reach definition methods based on hydraulic properties of rivers appear to lead to better discharge than reaches of arbitrary lengths
- Method for the detection of unlisted hydraulic structures compatible with future SWOT data are proposed and tested

Supporting Information:
- Supporting Information S1
- Data Set S1
- Data Set S2
- Data Set S3

Correspondence to:
R. P. d. M. Frasson,
frasson.1@osu.edu

Automated River Reach Definition Strategies: Applications for the Surface Water and Ocean Topography Mission

Renato Prata de Moraes Frasson[1] , Rui Wei[1], Michael Durand[1,2] , J. Toby Minear[3], Alessio Domeneghetti[4], Guy Schumann[5] , Brent A. Williams[6] , Ernesto Rodriguez[6] , Christophe Picamilh[7], Christine Lion[8], Tamlin Pavelsky[8] , and Pierre-André Garambois[9]

[1]Byrd Polar and Climate Research Center, Ohio State University, Columbus, OH, USA, [2]School of Earth Sciences, Ohio State University, Columbus, OH, USA, [3]Cooperative Institute for Research in Environmental Sciences, University of Colorado, Boulder, CO, USA, [4]School of Civil Engineering, University of Bologna, Bologna, Italy, [5]Remote Sensing Solutions, Inc., Monrovia, CA, USA, [6]Jet Propulsion Laboratory, California Institute of Technology, Pasadena, CA, USA, [7]Department of Hydraulics and Fluid Mechanics, INP – ENSEEIHT, Toulouse, France, [8]Department of Geological Sciences, University of North Carolina, Chapel Hill, NC, USA, [9]ICUBE-UMR 7357 Fluid Mechanics Team, INSA Strasbourg, Strasbourg, France

Abstract The upcoming Surface Water and Ocean Topography (SWOT) mission will measure water surface heights and widths for rivers wider than 100 m. At its native resolution, SWOT height errors are expected to be on the order of meters, which prevent the calculation of water surface slopes and the use of slope-dependent discharge equations. To mitigate height and width errors, the high-resolution measurements will be grouped into reaches (∼5 to 15 km), where slope and discharge are estimated. We describe three automated river segmentation strategies for defining optimum reaches for discharge estimation: (1) arbitrary lengths, (2) identification of hydraulic controls, and (3) sinuosity. We test our methodologies on 9 and 14 simulated SWOT overpasses over the Sacramento and the Po Rivers, respectively, which we compare against hydraulic models of each river. Our results show that generally, height, width, and slope errors decrease with increasing reach length. However, the hydraulic controls and the sinuosity methods led to better slopes and often height errors that were either smaller or comparable to those of arbitrary reaches of compatible sizes. Estimated discharge errors caused by the propagation of height, width, and slope errors through the discharge equation were often smaller for sinuosity (on average 8.5% for the Sacramento and 6.9% for the Po) and hydraulic control (Sacramento: 7.3% and Po: 5.9%) reaches than for arbitrary reaches of comparable lengths (Sacramento: 8.6% and Po: 7.8%). This analysis suggests that reach definition methods that preserve the hydraulic properties of the river network may lead to better discharge estimates.

1. Introduction

Assessing and predicting the availability of freshwater requires comprehensive measurements of river discharge and surface water storage, with sufficient spatial and temporal resolution to resolve the propagation of hydrological events through channels, floodplains, and lakes (Alsdorf & Lettenmaier, 2003). The global in situ network of gages does not entirely fulfil these requirements due to its heterogeneous spatial distribution, with varying density among different countries (Alsdorf et al., 2007) combined with data sharing barriers between nations (e.g., Gleason & Hamdan, 2015; Hossain et al., 2014; Sneddon & Fox, 2012; Wolf et al., 1999). With a planned launch in 2021, the upcoming Surface Water and Ocean Topography (SWOT) mission has the potential to fill gaps in the global streamgage network (Pavelsky et al., 2014) by providing freely available and spatially distributed observations of rivers wider than 100 m and lakes with an inundation area in excess of 62,500 m^2 (Biancamaria et al., 2015; Rodríguez, 2015). The anticipated benefits of this mission for surface water hydrology include: novel insights into the dynamics of water storage changes in lakes, reservoirs, and wetlands, and river discharge (Durand et al., 2010a), better understanding of the global water cycle and runoff processes (Pavelsky et al., 2014), easier monitoring of transboundary rivers (Biancamaria et al., 2011; Gleason & Hamdan, 2015; Hossain et al., 2014), simpler access to observations over remote areas assisting the management of reservoirs (Munier et al., 2015; Solander et al., 2016) and supporting flood modeling and forecasting (Schumann et al., 2010).

The core payload in the SWOT satellite is the Ka-band Radar Interferometer (KaRIn), which builds upon the Shuttle Radar Topography Mission (SRTM, described by Farr et al., 2007). SWOT will orbit Earth at an altitude

of 890.5 km with an inclination of 77.6° and repeat period of 20.86 days, during which most locations will be revisited between 1 and 3 times, with the revisitation frequency increasing with increasing latitude (Biancamaria et al., 2015). KaRIn will illuminate the surface with two 50 km swaths parallel to the ground track of the satellite and separated by a 20 km nadir gap. Inside each swath, the radar will resolve pixels at a native resolution varying from 60 m at the near range to 10 m at the far range and an along-track resolution of 6–7 m. (Biancamaria et al., 2015; Fjørtoft et al., 2014). The instrument will rely on the expected high contrast between water and land surfaces for water detection and on the phase difference between signals received by both antennas to construct interferograms, which combined with a terrain Digital Elevation Model (DEM) will allow the geolocation of pixels (Fjørtoft et al., 2014). More recently, Altenau et al. (2017) demonstrated the calculation of water surface heights and slopes from airborne Ka-band measurements from the AirSWOT platform, an airplane-mounted interferometric synthetic aperture radar, achieving root-mean-square errors of 9.0 cm and 1.0 cm km^{-1} for 10 km reaches for heights and slopes, respectively, over the Tanana River, located in Alaska.

Dingman and Bjerklie (2006) list a series of hydraulically meaningful variables that can be observed by satellite or aircraft-mounted instrumentation from which river discharge can be estimated. From this list, SWOT will be able to characterize water surface area, elevation, slope, changes in cross-sectional area, as well as channel morphology through indices such as sinuosity, meander length, and radius, whereas the remaining variables, i.e., velocity and depth, will have to be estimated. Four main families of methods will be used to estimate discharge based on SWOT data: data assimilation (e.g., Andreadis et al., 2007; Yoon et al., 2012), inversion of the Manning or other flow resistance equations (Durand et al., 2008; Durand et al., 2010b; Durand et al., 2014; Garambois & Monnier, 2015; Roux & Dartus, 2005; Yoon et al., 2016), scaling laws (Dingman, 2007; Gleason & Smith, 2014; Gleason et al., 2014; Leopold & Maddock, 1953), and by deriving channel resistance parameters by comparison with other known rivers (Bjerklie et al., 2003, 2005).

The application of Manning's equation requires the ability to estimate water surface slopes. LeFavour and Alsdorf (2005) evaluated the reach lengths necessary to resolve slopes in the presence of noise over areas of the Amazon basin. In their analysis, considering a minimum slope of 1.5 cm/km (Birkett et al., 2002) and a height error standard deviation of 5.51 m (LeFavour & Alsdorf, 2005), the minimum reach length need for the calculation of slope could be estimated by:

$$L = \frac{2\sigma}{S_{min}} \tag{1}$$

where L stands for the reach length in meters, σ for the height error standard deviation in meters, and S_{min} for the minimum slope in meters per kilometer, leading to a minimum reach length of 734 km.

The evaluation of the anticipated SWOT mission performance compiled by Esteban-Fernandez (2013) estimated a SWOT height error standard deviation of 4.4 cm when averaged over a 1 km^2 area and assessed the resulting slope uncertainty with:

$$\sigma_{slope}^2 = \frac{(2 \cdot \pi)^2}{12} 10^2 \cdot \sigma_h^2 \cdot \frac{1}{L^3 \cdot W} \tag{2}$$

where σ_h represents the height error standard deviation in cm based on an averaging area of 1 km^2 and L and W stand for reach length and width in km, respectively. Using the target values of 100 m for width, 1.4 cm/km for the slope standard deviation, and 4.4 cm for the height standard deviation listed in the science requirement documents (Rodríguez, 2015), the necessary reach length would be 6.9 km.

However, as described by C. Parker et al. (2012), the definition of the term "river reach" varies across disciplines, and often within the same discipline. C. Parker et al. (2012) classifies the different definition of reaches into two groups: operational, which are generally defined in terms of length, e.g., 500 m or a length equivalent to a number of channel widths, and functional, which define reaches based on distances over which a process of interest occurs. Within the functional category, the criterion or criteria used to define reach boundaries depends on how the resulting reaches are utilized. For example, Brenden et al. (2008) proposes an algorithm for reach definition that groups adjacent river segments into reaches based on similitude and tests the proposed methodology for river ecology studies. As the proposed use was for monitoring of river ecosystem, Brenden et al. (2008) evaluated the affinity of river segments based on seven

physicochemical river attributes that were descriptive of fish habitats. In a more recent study, Martínez-Fernández et al. (2016) designed a procedure for automatic reach definition to be applied to geomorphological studies. As the aim of the method was to define spatial units for the study of the river geomorphology, the chosen variables were valley slope, valley width, and active channel widths.

As our aim is discharge estimation, we focus on variables that are descriptive of hydraulic properties of the river. As shown for a braided river section of the Amazon basin with along stream altimetry data, the location of reach boundaries and the resulting reach lengths determine our ability to detect water surface slope variations, which reflect the balance between gravity and friction that drives free-surface flows (Garambois et al., 2017). Thus, Garambois et al. (2017) suggests the use of water surface slope spatial variability and the detection of inflection points on the water surface as criteria for river segmentation to be applied for the organization of altimetry data such as those provided by SWOT (Garambois et al., 2017).

As planform shape reflects river hydraulics, changes in planform descriptors are indicative of changes in hydraulic properties of rivers and could be used for reach definition. Leopold and Wolman (1960) suggested a connection between river hydraulics and plan view forms described by width of meander belts, channel sinuosity, and arc lengths, i.e., half of a meander wavelength. More recently, Bjerklie (2007) identified relationships between bankfull velocity and morphological descriptors such as meander wavelength, which can be estimated using satellite imagery. While the width of meander belts and meandering wavelength may be of difficult evaluation when the river planform deviates from a well-established sinusoidal pattern, sinuosity can be easily calculated and adjusted according to the length scale of interest, making it a good candidate for the definition of reaches.

The method used for the definition of river reaches may impact the quality of the discharge estimations by violating assumptions in the discharge equations, e.g., violating conservation of mass between contiguous reaches, including within its boundaries abrupt energy dissipation such as caused by dams or waterfalls, or by containing excessive observational uncertainty. While some reach boundaries are obvious, such as the location of major confluences, known waterfalls, dams, and other hydraulic structures, and for the specific case of SWOT, the swath boundaries, others are not easily recognizable without specialized data and human interaction, e.g., changes in channel bathymetry, changes in bed material leading to different flow resistance and planform characteristics, and others. Therefore, adequate reach definition strategies will, as well as possible, preserve the assumptions under which the discharge equations are derived and parameterized. Nevertheless, reaches should be long enough to allow for acceptable random errors associated with the observations derived from the chosen remote sensing platform.

Our work proposes two alternatives to utilize reaches of arbitrary lengths: the first based on the identification of inflection points on the water surface profile, which we assume to be associated with the location of hydraulic controls (Garambois et al., 2017; O'Loughlin et al., 2013), and a second method based on the identification of areas with similar sinuosity. Both methods are automated, requiring no further manual intervention after their initial configuration, which allows their application at global scale. Moreover, the methods are complementary. As the sinuosity method can be applied on centerlines derived from existing Landsat data, with a centerline delineation methodology such as described by Allen and Pavelsky (2015b), it can be used before the acquisition of new water surface elevation data and is suitable for the initial definition of reaches for a remote sensing platform such as SWOT. In contrast, the hydraulic controls method can be best applied to refine reaches once time series of water surface elevations are available and will allow detection of hydraulic structures not listed in prior databases.

We evaluate the performance of our reach definition and averaging methods in terms of reach-averaged water surface height, width, slope, and discharge root-mean-square errors. We compute reach-averaged errors by taking the differences between reach-averaged synthetic SWOT measurements and reach-averaged truths derived from the output of hydraulic models for the Sacramento and Po Rivers calculated as described in section 2.7. We discuss the similarities between the hydraulic control and sinuosity based methods in section 3.1 in terms of the proximity between reach boundaries identified by both methods. Sections 3.2.1, 3.2.2, and 3.2.3 present the evaluation of reach-averaged height, width, and slope errors, respectively, for the three reach definition methods as well as the evaluation of the impact of reach length on reach-averaged errors. Finally, section 3.2.4 discusses discharge errors caused by reach-averaged height, width, and slope errors.

2. Materials and Methods

2.1. Study Areas and Hydraulic Models

2.1.1. Sacramento River

The Sacramento River, near Colusa, CA, is a Mediterranean-climate river with a strong seasonal signal and distinct wet (November–May) and dry (June–October) seasons. The upper reaches of the Sacramento River are driven by substantial snowmelt runoff in early summer and infrequent large floods caused by large winter rain events, particularly those affecting the lower elevations of the watershed. There are significant dam-related hydrologic alterations, in particular the Shasta Dam (constructed in 1945), one of the ten largest dams in the United States, but also from numerous smaller dams and irrigation diversions along the length of the river (Kondolf & Batalla, 2005; Minear, 2010). During most flow conditions, levees constrict the river in the reaches downstream of Colusa, where the average river width varies from 80 to 100 m, whereas in the reaches upstream of Colusa, the levees are farther removed from the channel leading to an average width that ranges from 130 to 200 m depending on discharge.

For this study, we used a one-dimensional (1-D) hydraulic model of the study area released in 2013 by the California Department of Water Resources as part of the Central Valley floodplain evaluation and delineation program (Rogers, 2014). The geometry within the 1-D hydraulic model was created from topographic and bathymetric data collected in 2008–2010 from airborne LiDAR, and land- and boat-based surveys for the use in Central Valley floodplain evaluation and delineation program. Roughness coefficients were obtained by calibration using streamgage data collected during a high flow event from 2006 (Rogers, 2014). The resulting composite roughness coefficients considering main channel and floodplain varied from 0.02 to 0.071 s m$^{-1/3}$ in the upstream section of the Sacramento River, where levees are less prominent, whereas n varied from 0.025 to 0.035 s m$^{-1/3}$ downstream from Colusa, where the river is more confined to the main channel.

In the 1-D hydraulic model of the 155 km study area, there are 601 cross sections at an average spacing of 258 m, which corresponds to approximately 2.3 times average river width. To generate results for the SWOT hydrology simulator (described in section 2.2), the 1-D hydraulic model ran for 6 months, simulating discharges from 118 to 510 m^{3}s^{-1}. The Sacramento River study area alongside the evaluated SWOT swaths is depicted in Figure 1.

2.1.2. Po River

The Po River is the largest and longest Italian river, with a main stream length nearly equal to 650 km. The river basin has a catchment area of 70,090 km^2, which occupies almost entirely the Northern part of Italy. The Po River flows in the Eastern direction, from the Southern face of the Italian Alps to its delta in the Adriatic Sea. The river basin belongs to a Mediterranean climate zone, however, the hydrological regime of the river is influenced by 141 major tributaries, which flow from the Alps and Apennines and are subjected to unique orographic effects (Montanari et al., 2016). The river flows through the Po valley, one of the most economically developed areas in Italy with extensive human settlements, intense agricultural and industrial activity, and thus it has been strongly engineered to prevent floods. Referring in particular to the river stretch of interest for this study, i.e., from the gaging station of Borgoforte—45°03′N 10°45′E—to the beginning of the delta, the river is delimited by a system of earth embankments that constrain a stable main channel (200–500 m in width) and large floodplains characterized by widths that may vary up to 2.5 km.

The hydraulic behavior of the Po River is simulated by a quasi-two-dimensional hydraulic model with cross-sections built from a 2 m resolution LiDAR DEM (2005) integrated with boat surveys of the river (see Castellarin et al., 2011b, for more details). The Po River hydraulic model covered a river length of 133 km, which contained 111 cross-sections at an average spacing of 1.2 km, i.e., approximately 3 times average river width. Roughness coefficients were obtained through calibration using stage hydrographs observed at seven locations during the flood event of October 2000 and high water marks surveyed after the flood as described by Castellarin et al. (2011a). The roughness coefficient of the main channel varied in space but not in time, assuming 10 distinct values for the study area, which ranged from 0.044 s m$^{-1/3}$ (upstream section) to 0.025 s m$^{-1/3}$ (downstream section), whereas the floodplain n was assumed to be constant in space and time and equal to 0.1 s m$^{-1/3}$ (Domeneghetti et al., 2014). The hydraulic model of the Po River ran for 12 months, simulating discharges from 711 to 4,770 m^3 s^{-1}. Figure 2 shows the Po River study area alongside the analyzed SWOT swaths.
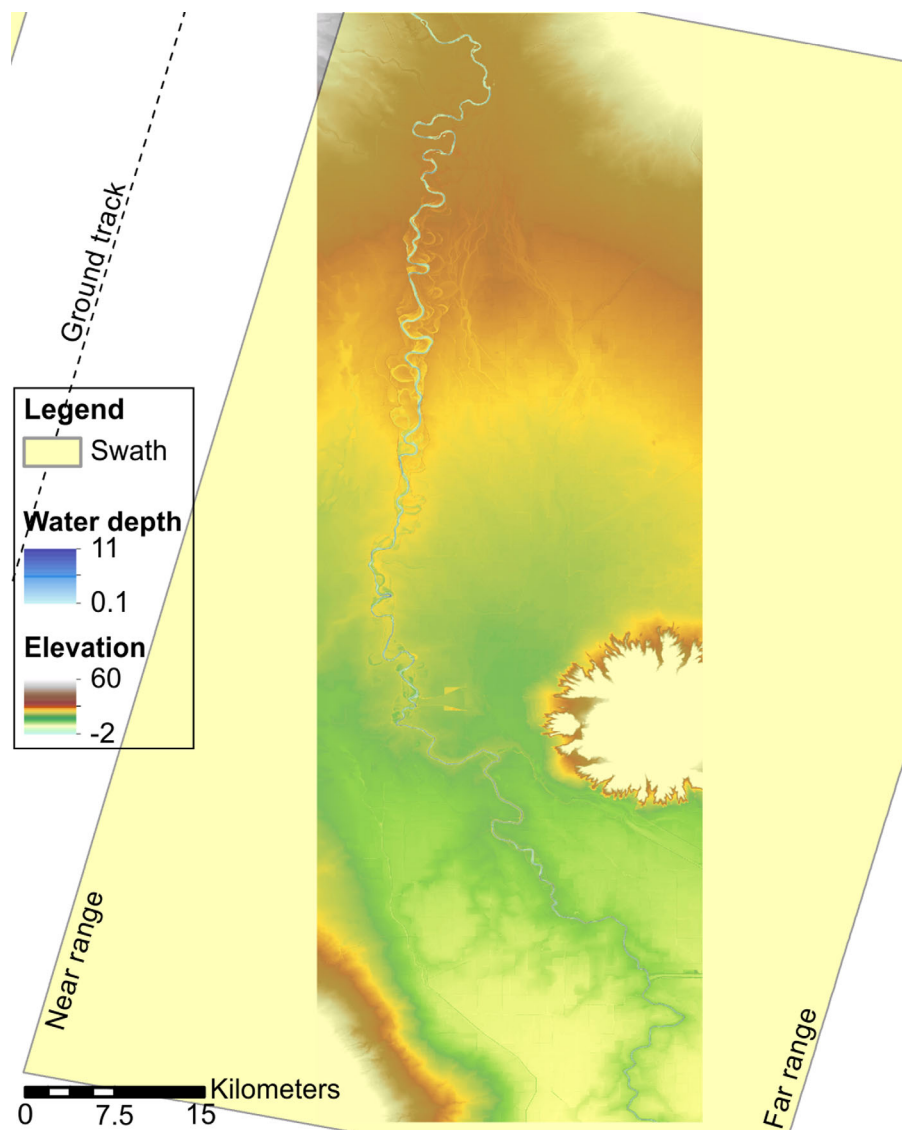
Figure 1. Sacramento River study area with the superimposed SWOT ground track (dashed line) and KaRIn swath. The Sacramento study area extends from 38°54′58″N to 39°45′14″N and from 122°4′19″W to 121°46′51″W.

2.2. SWOT Hydrology Simulator

The Jet Propulsion Laboratory (JPL) developed the SWOT hydrology simulator to generate synthetic SWOT measurements with realistic error characteristics. The SWOT simulator uses as inputs the DEM of the study area including water and land areas and a water mask. The water masks are two-dimensional maps that show which areas within the study area are inundated at the time of the simulated pass. Masks for each pass are built with the same resolution as the combined water-terrain DEM using inundation maps outputted by the hydraulic models at the closest time step to the time of the pass. The DEM of the area is built by superimposing the water surface maps outputted by the hydraulic models on the terrain DEM, such that if a pixel is inside the water mask, its height reflects the water surface height, whereas the heights of pixels located outside of the water mask correspond to the height of the terrain.

The simulator generates synthetic radar interferograms of the area, initially with no associated noise or measurement errors other than terrain layover. Subsequently, it simulates noisy interferograms by adding correlated circular Gaussian noise. The Gaussian correlation coefficient is determined by the interferometric coherence, which is modeled as a function of geometry, surface type scattering characteristics, and radar sensor parameters such as the signal-to-noise ratio. Additionally, the hydrology simulator can incorporate
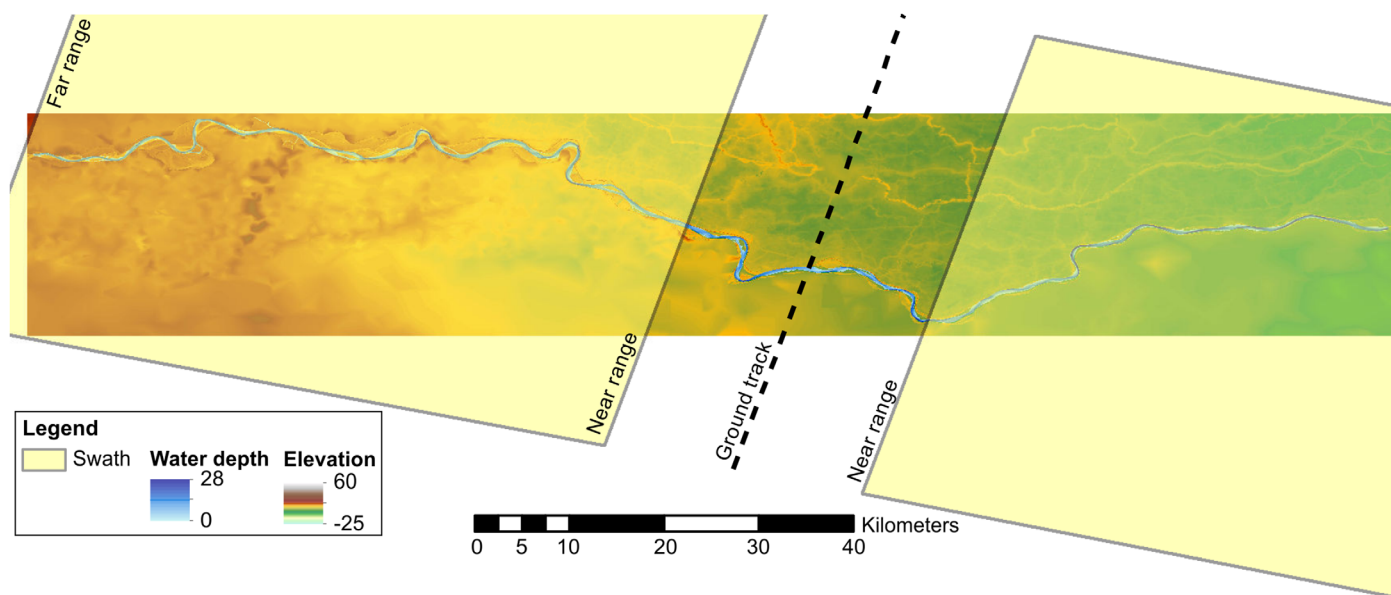
Figure 2. Po River study area with superimposed SWOT ground track (dashed line) and KaRIn swaths used in our study. The Po study area extends from 44°52′27″N to 45°5′4″N and from 10°44′55″E to 12°2′38″W.

attitude errors caused by spacecraft roll, and instrument errors. The simulator smooths the noisy interferogram through a process called "multilooking," in which four, as used in the present work, or more looks are used to reduce observational noise and build the multilooked interferogram. The multilooked power is then used for water detection, while the interferometric phase is used for height reconstruction and geolocation. Geolocation allows the construction of simulated pixel clouds, in which geolocated points with associated areas contain attributes including height and surface type, which can assume various classes, including interior water, water near land edge, and land near water (Figure 3a).

2.3. Processing of Simulated SWOT Data

Pixel clouds generated by the SWOT hydrology simulator are collections of all geolocated points, commonly referred to as pixels, obtained during a satellite overpass. These points are presented in a geographical coordinate system, i.e., longitude, latitude, and elevation above the ellipsoid, in our case, WGS84, and carry information on the surface area and type associated with the point. Figure 3a shows an example of a simulated pixel cloud generated over the Sacramento River and colored according to surface type. In order to allow the construction of water surface profiles and the application of one-dimensional discharge equations, the pixel cloud coordinate system must be simplified from its three-dimensional format to flow distances and water surface elevations, with the latter preferably being with respect to a geoid.

We executed this transformation using the RiverObs software package developed by the JPL. RiverObs translates the three-dimensional pixel cloud into a series of nodes located along the river centerline (shown in Figure 3b) containing node-averaged water heights and river widths in a process called vectorization. For the initial centerlines, we used the Global River Width from Landsat (GRWL) database (Allen & Pavelsky, 2015a) produced as described by Allen and Pavelsky (2015b). As RiverObs ingests a pixel cloud, it searches for water pixels located within a user-specified distance from the initial centerline. The centroid of the water pixels located within this search window can be used to improve the initial definition of the river centerline, in a process called centerline refinement. For the present work, we refined river centerlines using a low flow overpass, to avoid deviations in the centerline caused by out-of-bank flows or inundation of secondary channels, and then used this refined centerline for processing all passes.

Node-averaged widths and heights are calculated from water pixels located within the RiverObs search window. Water pixels found inside the RiverObs search window are assigned to their respective nearest node along the river centerline. The heights of the pixels are averaged to produce the node-averaged water
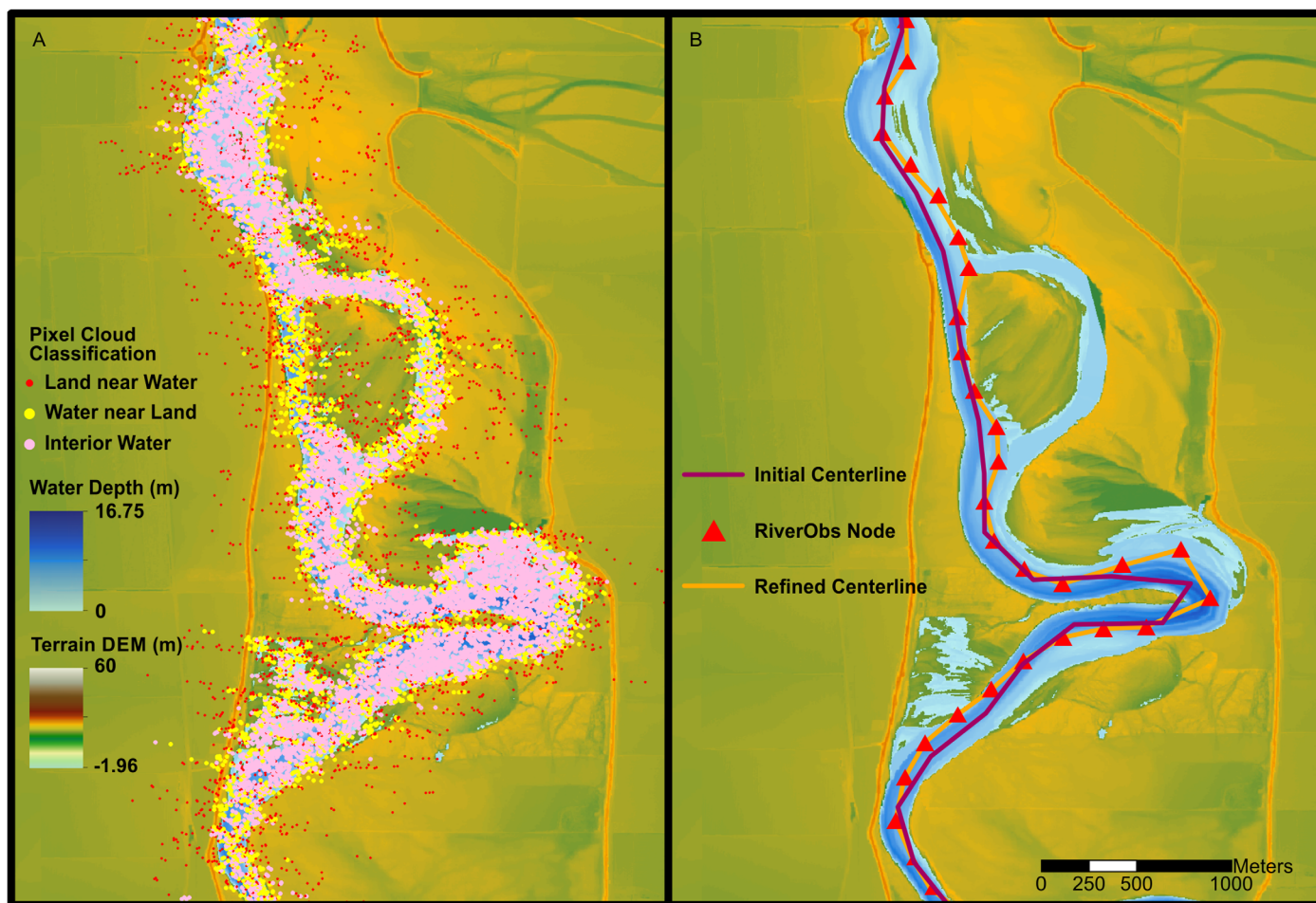
Figure 3. (a) Pixel cloud produced by the SWOT instrument simulator for a section of the Sacramento River. Pixel colors reflect their classification into: interior water (water pixels with water neighbors), water near land (water pixels with at least one land pixel neighbor), and land pixels. (b) River nodes produced by River-Obs, containing information on the average height and width of surrounding pixels, as well as their corresponding standard deviations.

surface elevation, whereas the inundated area associated with the selected pixels divided by the node distance is used to calculate the width at that node.

For the Sacramento River, we utilized a fixed search window of 400 m, which is 2 to 4 times the average channel width during the simulated period. For the Po River, we utilized 800 m (twice the average width) for all but the three highest flows, during which we increased the search window to 2,500 m, i.e., 4.5 times the average river width during the high discharge events. The vectorization of the pixel clouds covering the Sacramento and the Po Rivers yielded 747 and 582 nodes, respectively, which were spaced approximately 200 m apart.

2.4. River Reach Definition

We compared three different river segmentation strategies used to group RiverObs nodes into reaches: (1) reaches of arbitrary (fixed) lengths (section 2.4.1), (2) hydraulic control reaches (section 2.4.2), and (3) Sinuosity based reaches (section 2.4.3). In the first, we simply break up reaches at regular intervals measured along the rivers' centerlines. The second strategy consists of identifying hydraulic controls by searching for inflection points on the water surface profile (WSP). The third strategy takes into consideration river planform features, breaking up reaches according to channel sinuosity, defined here as the ratio between the river length measured along its centerline and the corresponding straight-line distance. Additionally, we added reach boundaries at intersections between the river centerlines and SWOT swaths. Following the definition of the reach boundaries, we calculated reach-averaged width, height, and slope (section 2.6).

2.4.1. Arbitrary Reach Definition Method

For this reach definition method, we segmented the river into reaches of equal, arbitrary lengths. Additional reach boundaries were located at SWOT swath boundaries, known hydraulic structures, and, if it were the case, location of major confluences. We tested different lengths for the arbitrary reaches, which we varied from 2 to 25 km to evaluate the impact of reach length on the accuracy of reach-averaged products. We evaluated the height and width errors obtained under the different reach lengths and contrast the estimated slope errors against the expected slope accuracies specified by the SWOT mission performance and error budget document (Esteban-Fernandez, 2013) for different reach lengths and river widths. Finally, we estimated the effects of errors on SWOT observations, i.e., reach-averaged heights, widths, cross-sectional area changes, and slopes into the reach-averaged discharge.

2.4.2. Hydraulic Controls Reach Definition Method

As with the arbitrary reach definition method, we placed reach boundaries at known hydraulic structures, confluences, and swath edges. Subsequently, we utilized simulated SWOT water surface height measurements to identify the location of hydraulic controls, which served as additional reach boundaries. The method builds upon the classification of gradually varied flow profiles presented by Chow (1959), which categorizes flow regimes based on the longitudinal profiles of the water surface and the channel bottom. According to the channel bottom slope, the profiles can be characterized as horizontal, mild, critical, steep, or adverse. These classes are further broken down into zones 1, 2, and 3, depending on the value of the actual depth with respect to the normal and critical depths. The locations where the channel class changes mark the location of hydraulic controls, which govern the upstream flow for subcritical flows (Froude number smaller than 1) or downstream for supercritical flows.

The exact classification of the flow profiles requires the determination of the normal, critical, and actual depths, which cannot be determined without in situ data. However, each type of flow profile is associated with a water surface concavity, which one can estimate from SWOT returns. We assume that for reaches with length scales on the order of kilometers and larger as defined in the SWOT science mission requirements (Rodríguez, 2015), the prevalent gradually varied flow classes are M1 (mild slope with actual depth greater than the normal depth) and A2 (adverse slope with actual depth greater than the critical depth). As shown in Figure 4, such simplification allows the differentiation between classes to rely solely on the sign of the second derivative of the water surface profile with respect to the flow distance, with concave profiles being classified as M1 and convex profiles as A2. Following this formulation, changes in concavity sign mark the location of hydraulic controls, which govern the upstream flow up to the previous control point, therefore representing ideal locations for the placement of reach boundaries.

The hydraulic controls method (hereafter referred as HC) comprises two main steps: the first is to identify unknown hydraulic structures by searching for backwater followed by sudden drops in the water surface elevation; the second step entails the search for transitions between flow profile types, marked by inflection points on the water surface profile. We ran the hydraulic structure identification and the flow classification routines using low flow overpasses, during which the WSP is more sensitive to changes in bathymetry.
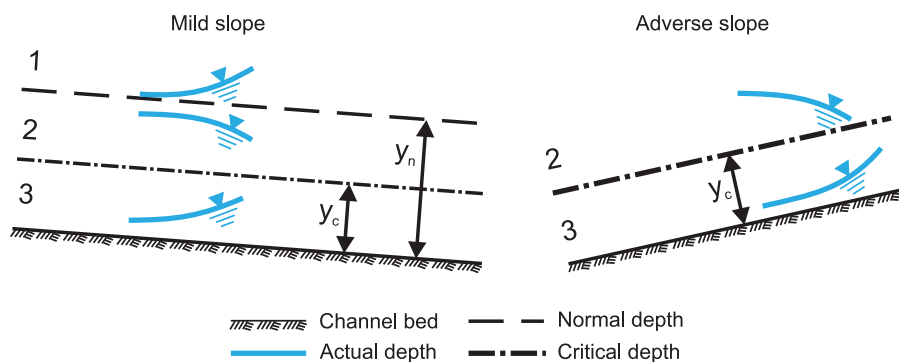

Figure 4. Idealized response of water surface profiles to the most frequently observed channel flow profiles. Adapted from Chow (1959) and Chin (2006).

In order to highlight the signature of hydraulic structures and the location of the WSP inflection points, we averaged node elevations among multiple low flow profiles. For the identification of hydraulic structures and the identification of inflection points on the WSP of the Sacramento River, we utilized the average of the six lowest discharge simulated SWOT overpasses, when discharges varied from 118 to 189 m^3 s^{-1}. For the Po River, we utilized three simulated SWOT overpasses for the classification of the water surface profile (discharges varying from 697 to 747 m^{3}s^{-1}). Although the Po River study area did not contain any dams or bridges, we still ran the hydraulic structure detection algorithm with the objective of assessing the possibility of false positives, a situation when the algorithm incorrectly detected nonexistent discontinuities on the WSP. For the assessment of false positives, we tested low flow profiles built using averages of 2–10 overpasses.

The identification of hydraulic structures consists of a search for backwater followed by sudden drops in water surface elevation. The procedure entails the execution of two separate linear regressions, the first using n nodes located upstream from the examined location and the second, using n nodes located downstream. We use both regression lines to predict the water surface elevation at the examined point and use:

$$y_{\text{sup}} = \hat{y} + t^* \cdot SE_{\hat{y}}$$
$$y_{\text{inf}} = \hat{y} - t^* \cdot SE_{\hat{y}}$$

(3)

to produce confidence intervals for the two predictions. In equation (3), y_{sup} and y_{inf} represent the superior and inferior limits of the confidence interval, respectively, $\hat{y}$ stands for the water surface elevation at the examined point (x^* along the longitudinal profile) predicted by the respective linear regression equation, t^* represents the value of the t-statistic for the desired confidence level and $n - 2$ degrees of freedom, and $SE_{\hat{y}}$ is the standard error for the prediction of $\hat{y}$, calculated by:

$$SE_{\hat{y}} = s \sqrt{1 + \frac{1}{n} + \frac{(x^* - \bar{x})^2}{\sum_{i=1}^{n} \left[(x_i - \bar{x})^2 \right]}}$$

(4)

where $\bar{x}$ represents the average flow distance of the subset of n nodes used in the construction of the confidence intervals and s is the regression standard error given by:

$$s = \sqrt{\frac{1}{n-2} \cdot \sum_{i=1}^{n} \left[(y_i - \hat{y}_i)^2 \right]}$$

(5)

In equation (5), n is the number of considered nodes, y_i is the observed water surface elevation at node i, and $\hat{y}_i$ is the predicted elevation at node i.

During the search for water surface drops, we built two subsets of 25 nodes, one located upstream and the second located downstream of the investigated location, each with a subset with a length similar to the chosen minimum reach length of 5 km, and an associated confidence interval of 85%. If the confidence intervals do not overlap, there is evidence that a discontinuity on the water surface profile exists at that location, in which case we check if the water surface slope upstream from detected discontinuity is flatter than the water surface slope downstream from the candidate location. Similar to the detection of discontinuities, we built 85% confidence intervals for the upstream and downstream slopes using equations (5) and (6), which are also employed in the identification of hydraulic controls. If the confidence intervals did not overlap and the slope downstream was steeper than the upstream slope, we flagged that location as a hydraulic structure. If contiguous discontinuities are identified, we select the location with the highest vertical drop. The positions of discontinuities are assumed to control the upstream flows and therefore are selected as reach boundaries.

In the following step, we search for hydraulic controls defined by changes in the sign of the second derivative of the water surface elevation with respect to flow distance (concavity) at each river node. Our method estimates the concavity at a node by taking the difference between the downstream and upstream slopes divided by the distance between the centroids of the up and downstream subsets of nodes. The number of nodes used in the subsets is determined by successively estimating confidence intervals (CI) for the upstream and downstream slopes and increasing the number of nodes until the slope CIs no longer overlap. We construct confidence intervals for the slopes of the upstream and downstream subsets using equation (5):

$$CI = b \pm t^* SE_b \tag{6}$$

where b stands for the linear regression slope, t^* is the value of the t-statistic for the desired confidence interval and $n - 2$ degrees of freedom, and SE_b represents the standard error of the least squares slope, which we calculate with:

$$SE_b = \frac{s}{\sqrt{\sum_{i=1}^{n}\left[(x_i - \bar{x})^2\right]}} \tag{7}$$

where s is estimated by equation (5).

If the two confidence intervals overlap, we assume that the two slopes are indistinguishable, therefore, we add $n/2$ nodes to both subsets and reevaluate their confidence intervals until they no longer overlap. Once the difference between slopes is statistically significant, we estimate the concavity c with equation (7):

$$c = \frac{b_{down} - b_{up}}{d} \tag{8}$$

where b_{up} and b_{down} are the up and downstream regression slopes and d is the flow distance between the centroids of the two subset of nodes. The regression slopes used in equation (8) do not have the same sign convention as river slopes as b_{up} and b_{down} are negative for decreasing elevations with increasing flow distances. For this analysis, we utilized an initial number of up and downstream nodes equal to 10 and a 95% confidence level for the computation of the regression slopes' confidence intervals.

Subsequently, we search for sign reversals in the water surface concavity, which combined with the location of hydraulic controls and swath boundaries constitute the reach boundaries. As a last step, we impose minimum reach length requirements. Initially, we sort reaches by length and check if the shortest reach meets the reach length requirements. If the shortest reach is shorter than a minimum reach length of 5 km, we check which of its immediate neighbors has an average concavity closer to the reach in question, to which the short reach is merged. The reaches are resorted by length and the procedure is repeated until reaches meet the minimum length requirements. The exceptions to the minimum reach length requirements are boundaries defined by hydraulic structures and swath boundaries.

The HC method is automated. Once the confidence intervals, the number of nodes, and overpasses for the identification of hydraulic structures and transition between flow profile classes and the minimum reach length are set, no human inputs are required. A prototyped algorithm for the HC method is included with this manuscript as supporting information (S1).

2.4.3. Sinuosity Reach Definition Method

The sinuosity method allows the definition of reach boundaries based solely on the examination of the river centerline, which can be delineated with existing data, such as Landsat imagery, or the method can make use of refined centerlines once SWOT data are available. As the sinuosity method does not require SWOT observations, it can be applied before the beginning of the mission and it offers the possibility of expediting initial releases of reach-averaged SWOT products. The method has three inputs: river centerline, SWOT swaths, and an optional input of known hydraulic structures. Essentially, the method searches for areas with similar sinuosity subjected to a minimum reach length, in addition to placing reach boundaries at locations where the centerline crosses swath boundaries and at known hydraulic structures and confluences.

Similar to Leopold & Wolman (1957), we defined sinuosity as the ratio between river length and downvalley length, which is computed with equation (8):

$$S_k = \frac{\sum_{i=-\frac{m}{2}}^{\frac{m}{2}-1} \sqrt{(No_{k+i+1} - No_{k+i})^2 + (E_{k+i+1} - E_{k+i})^2}}{\sqrt{\left(No_{k+\frac{m}{2}} - No_{k-\frac{m}{2}}\right)^2 + \left(E_{k+\frac{m}{2}} - E_{k-\frac{m}{2}}\right)^2}} \tag{9}$$

where S_k stands for the sinuosity at the node k, m stands for the number of nodes used in the computation, where if $m/2$ is not an integer number, it is rounded toward minus infinity, No stands for the northing and E for the easting according to the appropriate conformal projection. The number of nodes used for the

sinuosity computation depends on the minimum reach length and the average width of the river. We calculated m by ensuring that flow distance covered in the sinuosity computation matched the minimum reach length or at least of 10 times the bankfull width of the river as suggested by Kiel (2015). The minimum reach length of 5 km under a node spacing of 200 m led to the use of 25 nodes. For both the Po and the Sacramento Rivers, the minimum reach length was the determining factor in the estimation of the number of nodes used in the computation of the sinuosity.

We defined areas of similar sinuosity as the locations between local maxima or minima of the first derivative of the sinuosity with respect to flow distance, which we identified by searching for sign reversals in the second derivative of sinuosity with respect to flow distance. As with the Hydraulic controls method, the first and second derivatives of channel sinuosity are calculated with equations (3) and (4), respectively, considering upstream and downstream subsets of nodes as long as the minimum reach length of 5 km. Subsequently, we imposed the minimum reach length of 5 km by merging the shortest reaches with one of their neighbors, either the immediately up or downstream reach. Similar to the HC merging method, the selection of which neighbor to use depended on whether the upstream or downstream sinuosity was more similar to the sinuosity of the merging reach. The merging procedure was repeated until all reaches had lengths greater than or equal to the specified minimum reach length. Nevertheless, reaches defined by swath boundaries and known hydraulic structures were not subject to the minimum reach length criterion. A prototyped algorithm for the sinuosity method is included with this manuscript as supporting information (S2).

2.5. Water Surface Smoothing

We applied two different methodologies to mitigate the noise observed in the simulated SWOT measurements of heights at the node level. The first, which we applied in conjunction with the arbitrary reach definition scheme, entails the use of a moving average window with the same length as the reach length and with Gaussian weights to smooth node heights. In this methodology, all nodes lying 5 km upstream or 5 km downstream from the current node contribute to the calculation of that node's height. The Gaussian curve used to assign the weight to each node property was adjusted such that a node located 2 km up or downstream from the center of the window would correspond to being located one standard deviation away from the center of a standard normal curve.

The second methodology, used in conjunction with sinuosity and hydraulic controls reach definition schemes, consists of using an adaptive Gaussian averaging window to smooth node heights. The method changes the Gaussian average window to match the length of the reach that contains the central node. Additionally, we set the Gaussian window standard deviation to 1/5 of the reach length, with a minimum of 1 km. Using the adaptive window size provides a compromise between decreasing data noise and preserving the shape of the water surface profile. Although the adaptive Gaussian window allows the use of information from nodes located outside of the reach, the averaging window is not allowed to cross boundaries defined by hydraulic structures.

2.6. Reach Averaging

We calculated reach-averaged heights by averaging the smoothed heights of nodes contained within reach boundaries and estimated the reach-averaged widths by dividing the inundated area in a reach by the reach length. Subsequently, we obtained reach-averaged slopes by dividing the elevation lost throughout the reach by the reach length. For the estimation of the reach-averaged cross-sectional area, we proceeded as in Durand et al. (2014). We express the cross-sectional area of the reach i, during the overpass j, $A_{i,j}$, in terms of the reach's cross-sectional area below the minimum recorded elevation, $A_{i,o}$, and the associated change in cross-sectional area between the minimum recorded stage and the overpass j ($\delta A_{i,j}$), which leads to:

$$A_{i,j} = A_{i,0} + \delta A_{i,0} \tag{10}$$

The cross-sectional area formulation expressed in equation (10) is convenient, as it separates $A_{i,j}$ into an element that cannot be observed with SWOT ($A_{i,o}$) and the areal change ($\delta A_{i,o}$), which can be estimated directly from SWOT observations. If $y_{i,j}$, and $w_{i,j}$, are the reach-averaged water surface elevation and width for the reach i during overpass j and $y_{i,0}$ and $w_{i,0}$ are the reach-averaged water surface elevation and width for the same reach during the minimum recorded elevation, then $\delta A_{i,j}$ can be estimated with:

$$\delta A_{i,j} = \frac{w_{i,0} + w_{i,j}}{2} \cdot \left(y_{i,j} - y_{i,0} \right) \tag{11}$$

The estimation of $A_{i,o}$ and the effective Manning's roughness coefficient for a reach, named $\tilde{n}$ as in Durand et al. (2014), is more complex than previously mentioned reach-averaged quantities, as they cannot be derived directly from SWOT measurements. During the SWOT mission, unobservable parameters such as $\tilde{n}$ and $A_{i,o}$ needed for the computation of discharge will be estimated through one or more algorithms. Among the existing discharge algorithms whose performance was assessed by Durand et al. (2016), GaMo (Garambois & Monnier, 2015), MetroMan (Durand et al., 2014), and mean flow and constant roughness algorithm (MFCR method is similar to the framework presented in Smith et al., 2015) estimate both $A_{i,o}$ and $\tilde{n}$ (with the exception of MFCR that uses a constant $\tilde{n}$) with the purpose of calculating reach-averaged discharges.

To untangle the uncertainties inherent to the different discharge algorithms from the effects of reach definition strategies, we opted to use cross-sectional areas taken from the Sacramento River and the Po River hydraulic models during the minimum recorded elevation to estimate the $A_{i,o}$. Additionally, we used discharge, width, slope, and cross-sectional area computed from the hydraulic models for each reach and for each overpass to estimate the corresponding effective roughness coefficient. We estimated $\tilde{n}_{i,j}$, the effective roughness coefficient for the reach i during overpass j, by solving Manning's equation for $\tilde{n}_{i,j}$:

$$\tilde{n}_{i,j} = \frac{1}{Q_{i,j}} \cdot \left(A_{i,0} + \delta A_{i,j} \right)^{5/3} w_{i,j}^{-2/3} S_{i,j}^{1/2} \tag{12}$$

and using the true reach-averaged values of width ($w_{i,j}$), area ($A_{i,o} + \delta A_{i,j}$), water surface slope ($S_{i,j}$), and discharge ($Q_{i,j}$).

Subsequently, we used the estimated $\tilde{n}_{i,j}$, $A_{i,o}$, alongside synthetic measurements of reach-averaged width $\hat{w}_{i,j}$, water surface slope $\hat{S}_{i,j}$, and change in cross-sectional area $\delta\hat{A}_{i,j}$ to calculate reach-averaged discharges $\hat{Q}_{i,j}$. For the discharge estimation, we used Manning's equation, assuming that the friction slope can be approximated by the water surface slope and that the reach-averaged width is much larger than the depth, reducing the wetted perimeter to the value of the river width. Under such assumptions, Manning's equation can be written as:

$$\hat{Q}_{i,j} = \frac{1}{\tilde{n}_{i,j}} \cdot \left(A_{i,0} + \delta\hat{A}_{i,j} \right)^{5/3} \hat{w}_{i,j}^{-2/3} \hat{S}_{i,j}^{1/2} \tag{13}$$

where, variables accompanied by the hat symbol denote values derived from the synthetic SWOT observations, with the exception of discharge, as it also depends on the unobservable values of $\tilde{n}_{i,j}$, $A_{i,o}$. A prototyped algorithm for reach averaging is included with this manuscript as supporting information (S3).

2.7. Error Metrics

We evaluated the performance of the reach definition methods in terms of root-mean-square errors (RMSEs) computed per overpass ($RMSE_T$, equation (13)) and per reach ($RMSE_L$, equation (14)). For the computation of the per pass $RMSE_T$, we considered differences between reach-averaged synthetic SWOT measurements and reach-averaged values computed from the river models, resulting in one RMSE value per overpass per river. We calculated the $RMSE_T$ for an overpass j with:

$$RMSE_{T,j} = \sqrt{\frac{1}{N_{r,j}} \sum_{i=1}^{N_{r,j}} \left(\hat{v}_{i,j} - v_{i,j} \right)^2} \tag{14}$$

where $\hat{v}_{i,j}$ is the evaluated variable (height, slope, and discharge) at reach i and overpass j, $N_{r,j}$ is the number of reaches observed during the overpass j, and $v_{i,j}$ is the reach-averaged truth calculated from the hydraulic simulation of the river for the evaluated variable at the reach i and overpass j.

The $RMSE_L$ accounted for errors across the N_{over} overpasses, producing one error estimate for each reach, which we used for the analysis of impacts of reach length into reach-averaged products. The $RMSE_L$ for each reach i was computed with:

$$RMSE_{L,i} = \sqrt{\frac{1}{N_{over}} \sum_{j=1}^{N_{over}} (\hat{v}_{i,j} - v_{i,j})^2} \tag{15}$$

where $\hat{v}_{i,j}$ is the evaluated variable (height, slope, width, and discharge) at reach i and overpass j.

We assessed reach-averaged width errors and the impact of reach-averaged height, width, cross-sectional area change, and slope errors into discharge in terms of relative RMSE (rRMSE) using equations (15) and (16):

$$rRMSE_{T,j} = \sqrt{\frac{1}{N_{r,j}} \sum_{i=1}^{N_{r,j}} \left(\frac{\hat{v}_{i,j} - v_{i,j}}{v_{i,j}}\right)^2} \tag{16}$$

$$rRMSE_{L,i} = \sqrt{\frac{1}{N_{over}} \sum_{j=1}^{N_{over}} \left(\frac{\hat{v}_{i,j} - v_{i,j}}{v_{i,j}}\right)^2} \tag{17}$$

Similarly to $RMSE_T$ and $RMSE_L$, $rRMSE_T$ and $rRMSE_L$ represent an aggregation of errors in space and time, respectively.

3. Results and Discussion

3.1. Comparison of the Reach Definition Strategies

Several authors have established relationships between river planform, cross-sectional geometry, and water surface profile shape (e.g., Ikeda, 1984; Ikeda et al., 1981; Odgaard, 1986; Odgaard & Abad, 2008; G. Parker et al., 1983; Rosgen, 1994). Therefore, we expected to observe some correspondence between boundaries identified by sinuosity and by hydraulic controls. Table 1 presents the minimum, mean, and maximum reach lengths under the HC and sinuosity method, demonstrating that in terms of reach length statistics, both methods lead to similar outcomes. There are also similarities in the location of reach boundaries generated by both methods. Table 2 summarizes the comparison between reach boundaries defined by sinuosity and HC methods by computing how many reach boundaries were located within 1, 2, and 3 km of each other, with distances measured along the centerlines of the rivers. Table 3 shows the locations of the hydraulic structures included in the Sacramento River model.

Comparing the reach boundaries identified by the sinuosity and the HC methods for the Sacramento River (Figures 5a–5c), we see correspondences at 0, 12.4, 54.0, 60.0, 82.5, 89.0, 137.2, and 151.8 km, where reach boundaries defined by both methods are located within 1 km of each other. From this list, only three boundaries were defined by the swath's edge, i.e., 0, 117, and 151.8 km, indicating that SWOT might be able to observe connections between river sinuosity and hydraulic characteristics of rivers. Coincidences between river boundaries defined by both methods occur more frequently in the first 90 km of the Sacramento River, where the channel slope is steeper and concavities in the water surface profile are more pronounced than on the downstream section of the river. While decreasing the minimum reach length for the HC and sinuosity routines from 5 to 2 km increases the number of coinciding boundaries, leading to 20 coincidences (within 1 km) out of a total of 40 boundaries defined using inflection points in the WSP and sinuosity, the shorter reach lengths would result in higher height, width, and slope errors.

The correspondence between the two methods was not as good for the Po River (Figures 5d–5f and Table 2) when using the adopted minimum reach length of 5 km. The correspondence between the HC and the sinuosity methods appears to be affected by the minimum reach length. For example, decreasing the minimum reach length requirements from 5 to 2 km led to a considerable increase in the similarity between reach boundaries defined by both methods. After the decrease, on the upstream swath of the Po River, 11 boundaries defined by inflection points in the WSP and sinuosity profiles were within 1 km of each other, which corresponds to 55% of the reach boundaries under the shorter minimum reach length requirements. The

Table 1
Comparison of Reach Lengths Originated From the Sinuosity and Hydraulic Controls Reach Definition Strategies

River	Minimum reach length (km)	Mean reach length (km)	Maximum reach length (km)
Sinuosity			
Po	5.0	8.4	13.4
Sacramento	5.7	8.9	16.2
Hydraulic controls			
Po	5.4	9.1	14.0
Sacramento	5.2[a]	8.3	14.6

[a]The Sacramento River, under the HC method had two reaches under the minimum reach length, one with a length of 1 km and a second with a length of 4.9 km caused by swath edges and one detected structure.

Table 2
Comparison of the Locations of the Sinuosity and Hydraulic Controls Defined by Inflection Points in the Sinuosity and Water Surface Profile, respectively

River	Within 1 km	Within 2 km	Within 3 km
	Sinuosity and HC boundaries located		
Po	3	5	7
Sacramento	6	8	10
	Fraction of number of reaches		
Po	27%	45%	64%
Sacramento	40%	53%	67%

Note. The HC method identified 15 reaches for the Sacramento River and 11 for the Po River due to inflection points in the WSP. The sinuosity method identified 15 reaches for the Sacramento River and 12 reaches for the Po River due to inflection points in the sinuosity profile. This table does not consider reach boundaries due to Swath edges, as they are identical for all methods by definition

downstream swath saw little improvement in the correspondence between river segmentation methods, likely due to the smaller variation in both sinuosity and in water surface concavity, which implies weaker hydraulic controls.

3.2. Evaluation of the Simulated Reach-Averaged Products
3.2.1. Height

The overpass-based $RMSE_T$ revealed that height errors depend on discharge for both Sacramento (Figure 6a) and Po (Figure 6b) Rivers, with increasing discharges leading to smaller $RMSEs$. The decrease in $RMSE_T$ can be partially explained by decreasing biases observed during the higher discharges shown in Figures 6e and 6f for the Sacramento and Po Rivers, respectively. Higher biases during lower discharges that disappear as water level rises are an indication of terrain layover, a situation when the radar return from the water surface and the surrounding terrain reach the satellite simultaneously. As the returns from the different targets are registered at the same time, the targets become indistinguishable, effectively obscuring the lower elevation targets, and potentially leading to positive biases, i.e., overestimation of the water elevation.

Terrain layover is more likely to occur when a terrain feature such as levees bordering a river have a slope higher than the local sensor look angle. Whether a terrain slope will lead to layover depends on the orientation of the river with respect to the swath and on the position of the target with respect to the swath, i.e., slope greater than 0.6° in the near range or greater than 3.9° in the far range, (Fjørtoft et al., 2014). As the water level increases, the difference in elevation between the levees and the water surface decreases, diminishing the impact of terrain on the estimation of the target's elevation. The higher height biases observed on the Sacramento River as opposed to those observed on the Po River (Figures 6e and 6f) illustrate the effect of the orientation of the river with respect to the swath. Levees running in parallel to the swath are at the most disadvantageous conditions, as is the case for a considerable fraction of the Sacramento River (Figure 1), whereas levees perpendicular to the swath, as is the case of the Po River (Figure 2) have considerably smaller layover effects.

We further examined the possibility of terrain layover causing the height biases by excluding pixels classified as "water near land edge," i.e., a water pixel with at least one neighbor classified as land, and computing node height only from pixels identified as "interior water," i.e., a water pixel surrounded only by other water pixels. The exclusion of water near land edge pixels was effective in remediating the overestimation of the Sacramento River water surface elevation. As interior water pixels are less likely to contain mixed land and water returns, they are less prone to layover errors. Therefore, the observed decrease in height biases when using only interior water pixels is an indication that terrain layover caused a substantial part of the observed overestimation of the water surface elevation particularly during low flow conditions. However, we identified two major consequences of the exclusion of water near land edge pixels: (1) some nodes (11 during the lowest flow condition, 7 during average flow, and 1 during the highest discharge) had no

Table 3
Location of the Head Losses Present in the Sacramento River Study Area

Water surface elevation (m)					
Upstream	Downstream	Drop (m)	Latitude	Longitude	Notes
39.03	38.9	0.13	39°45′04″N	121°59′49″W	Highway 32 bridge by Hamilton City
29.75	29.6	0.15	39°37′45″N	121°59′31″W	Old ferry road bridge by Ordbend
21.32	21.19	0.13	39°27′26″N	121°59′42″W	Biggs-Willows road bridge
12.81	12.51	0.30	39°12′51″N	122°W	River road bridge at Colusa
11.82	10.92	0.90	39°08′45″N	121°55′05″W	State highway 20 bridge at Meridian

Note. The water surface elevation drops were in respect to the day 23, the lowest flow in the simulated period, with an average discharge of 118 m³ s⁻¹.
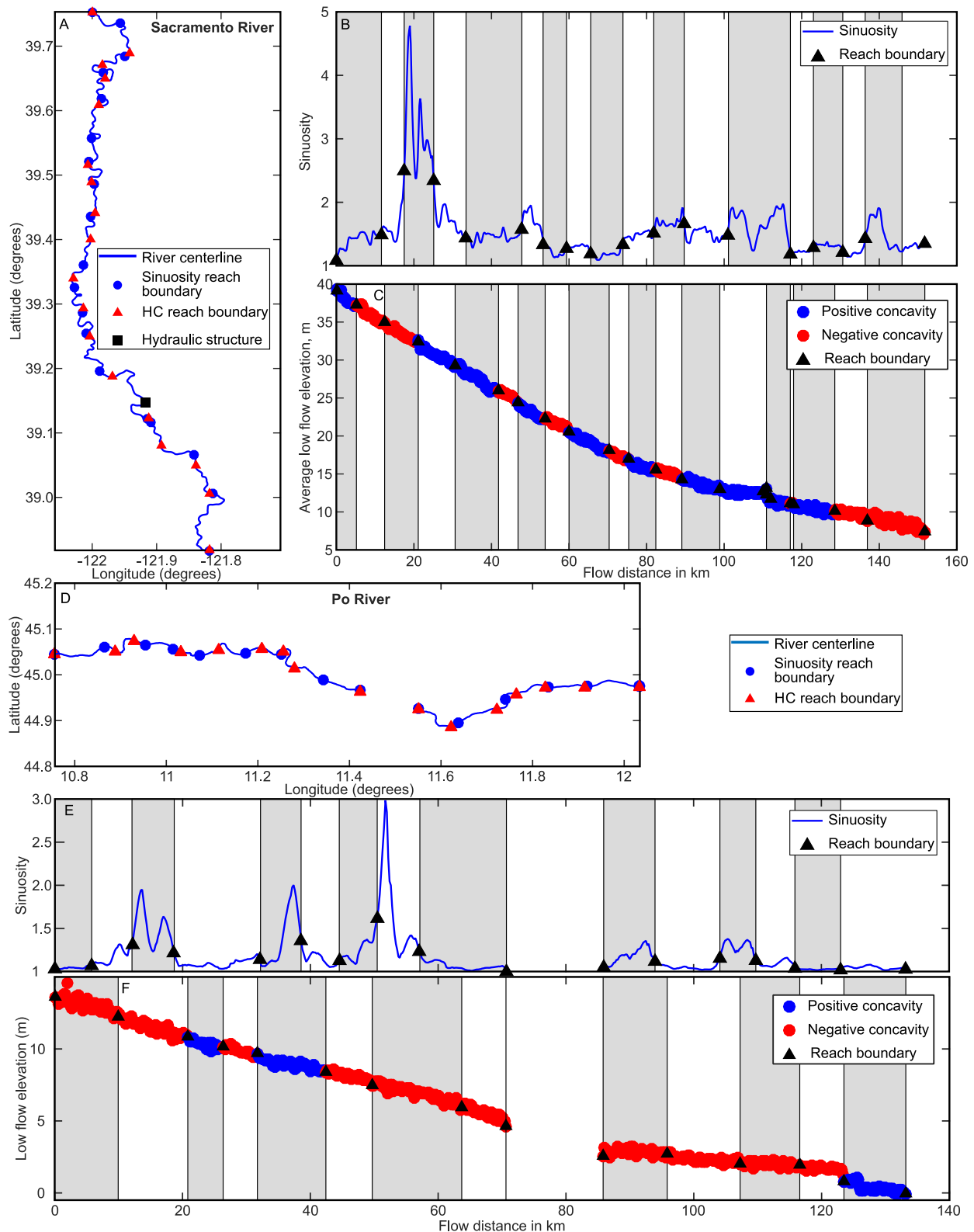
Figure 5. (a) Sacramento River centerline with superimposed location of hydraulic structures, hydraulic control reaches, and sinuosity reaches. (b) Sacramento River sinuosity and locations of the river reach boundaries. (c) Sacramento River's water surface profile with color-coded concavity signals. (d) Po River centerline with reach boundaries. (e) Po River sinuosity and the location of river reach boundaries. (f) Po River's water surface profile with color-coded concavity signals. Succession between white and grayed areas in Figures 5b, 5c, 5e, and 5f denote different reaches. The discontinuity in Figures 5d–5f occurs due to the swath gap, as shown in Figure 2.
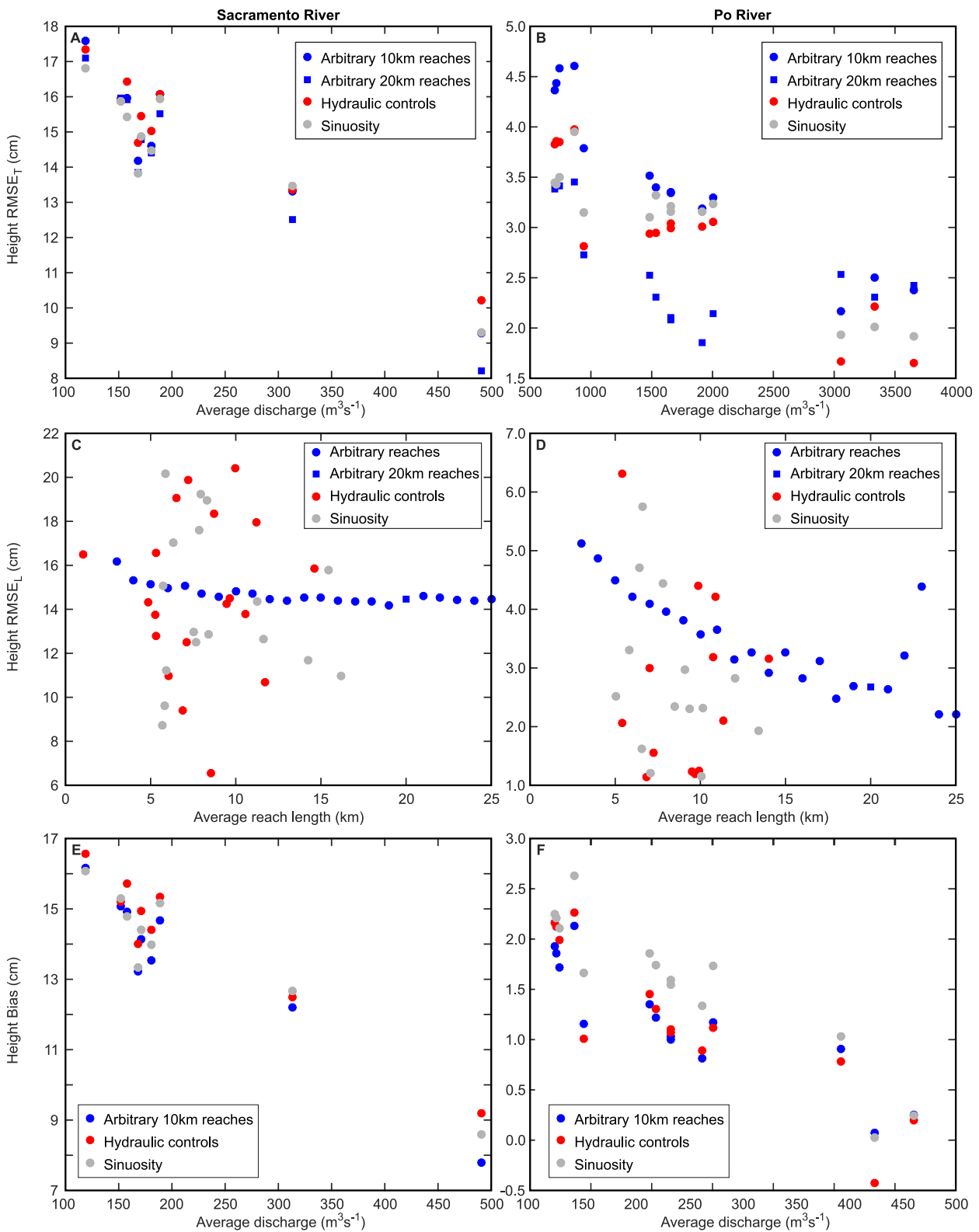
Figure 6. (a) Reach-averaged height *RMSE* computed for all reaches with length greater than 3 km for each one of the nine overpasses at the Sacramento River versus the average discharge during the overpass. (b) Reach-averaged height *RMSE* computed for all reaches with length greater than 3 km for each one of the 14 overpasses at the Po River versus the average discharge during the overpass. (c) Time-averaged *RMSE* of reach-averaged heights at the Sacramento River versus reach length. (d) Time-averaged *RMSE* of reach-averaged heights at the Po River versus reach length. (e) Height bias versus average discharge for the Sacramento River. (f) Height bias versus average discharge for the Po River.

valid height measurements and (2) as fewer points are available for averaging, the random component of the error increases.

Comparing the Sacramento River reach-averaged height $RMSE_T$ (Figure 6a) produced with the arbitrary 10 km reaches, sinuosity, and HC methods, we see that despite the shorter average reach lengths generated by the sinuosity and the HC methods (Table 1), the three methods had comparable performances. During low flows, the sinuosity method, which applies an adaptive Gaussian window moving average to smooth the water surface, had slightly better performance than the arbitrary 10 and 20 km reaches. For the Po River, both HC and sinuosity methods outperformed the arbitrary 10 km reaches and, during high flow, the arbitrary 20 km reaches.

Figures 6c and 6d show the effect of reach length on the reach-averaged height $RMSE_L$ for the Sacramento and the Po Rivers, respectively. Analyzing the behavior of the arbitrary reach definition methodology, we see that increasing reach length decreases $RMSEs$ for both rivers. Decreasing errors with increasing reach lengths is not as visible on the Sacramento River (Figure 6c), as random errors are much smaller than systematic errors for this river, especially during lower discharges. This is expected, as averaging effectively reduces the random component of the error, while leaving the biases unmitigated. Figures 6c and 6d also show that there is a limit to how much of the random errors can be eliminated through the increase of reach length and that this limit is reached faster for the Sacramento River ($\sim$15 km) than for the Po River ($>$25 km).

The analysis of the impact of reach length on the reach-averaged height $RMSE_T$ produced by the sinuosity and the hydraulic controls method is more difficult as these methods generate reaches with different reach sizes. However, it appears that both methods show a trend of decreasing height errors with increasing reach lengths. Moreover, Figures 6c and 6d appear to indicate that as reach length increases, height errors tend to become more stable and predictable.

3.2.2. Width

With respect to reach lengths, reach-averaged width errors behaved similarly to reach-averaged heights. As the reach length increased, the relative $RMSE_L$ ($rRMSE_L$) decreased with most of the benefit in increasing the reach length being achieved at approximately 10 km (Figures 7a and 7b). The Po River showed a similar decrease in width $rRMSE_L$ up to 15 km, after which this error metric became less descriptive (Figure 7b). Figures 7c and 7d show a direct comparison of simulated SWOT reach-averaged widths and true widths for all synthetic overpasses.

An accurate comparison between inundated width as potentially observed by SWOT and the cross-sectional "wetted" width as produced by a 1-D hydraulic model, e.g., top width in HEC-RAS, is not straightforward. The two parameters are not always commensurate in hydrodynamic terms. Complications arise due to a multitude of reasons including: the discrete width sampling at the hydraulic model cross sections, which can overemphasize or underemphasize the inundated floodplain, mismatches in the location of the centerlines leading to different definitions of width, nonlinear cross sections in the hydraulic model, and others. A more direct comparison could be derived by overlaying inundated area, or width thereof, as observed by SWOT with that simulated by a 2-D flood inundation model. However, such an evaluation is only tangentially relevant to the evaluation of reach definition strategies and outside of the scope of the present work.

3.2.3. Slope

Compared to height and width, overpass-based reach-averaged slope errors ($RMSE_T$) were more robust with respect to discharge for both Sacramento and Po Rivers (Figures 8a and 8b). For both Po and Sacramento Rivers, reach-averaged slopes produced by the sinuosity method were considerably better than those generated by the arbitrary 10 km reaches method, despite having shorter average reaches. For the Sacramento River, HC and arbitrary 10 km reaches slopes were comparable, whereas for the Po River, HC and sinuosity slopes were comparable to each other and both where considerably superior to arbitrary 10 and 20 km slopes.

As expected, slope errors showed a strong relationship with reach length (Figures 8c and 8d). The SWOT mission performance error budget document (Esteban-Fernandez, 2013) states that, in the absence of layover errors, error variance (σ^2_{slope}) can be predicted by equation (2). Although the equation that describes slope dependency on river width and reach length presented in the science requirements document
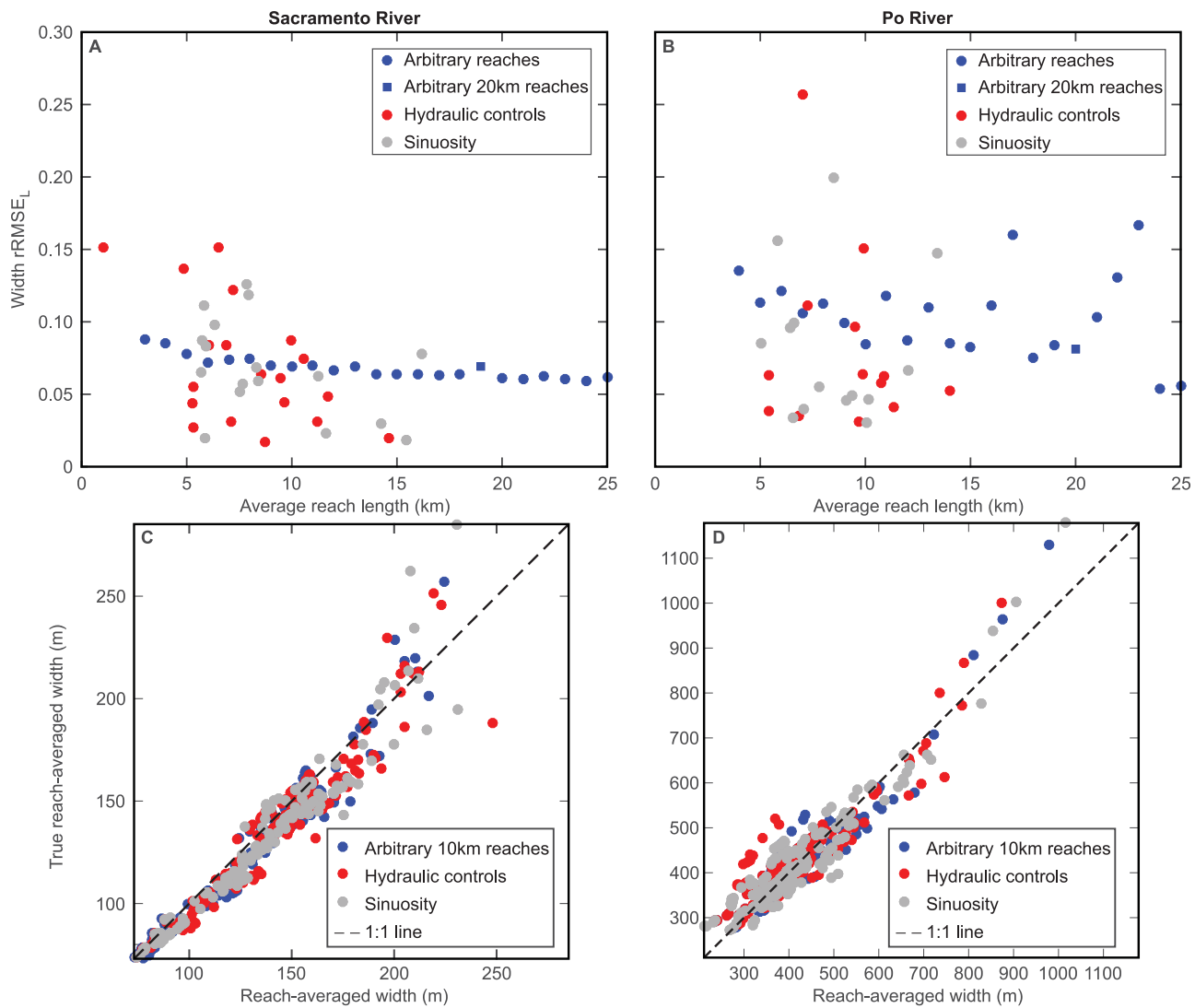
Figure 7. (a) Time-averaged *rRMSE* of reach-averaged width at the Sacramento River versus reach length. (b) Time-averaged *rRMSE* of reach-averaged width at the Po River versus reach length. (c) Reach-averaged widths versus true reach-averaged widths for the Sacramento River. (d) Reach-averaged widths versus true reach-averaged widths for the Po River.

(Rodríguez, 2015) supersedes equation (2), we chose to compare our slopes with the older equation, as it was derived assuming height smoothing and is, therefore, more compatible with our methodology than the newer equation presented by Rodríguez (2015). Even though $RMSE_L$ reflects a combination of bias and random errors, sinuosity and HC slope $RMSE_L$ were mostly the same or below the slope error standard deviation (σ_{slope}) calculated from the square root of equation (2) (Figures 8c and 8d).

3.2.4. Discharge

Figure 9 shows how height, width, and slope errors propagate into discharge for the different reach definition strategies. Figures 9a and 9b show how discharge $rRMSE_T$ respond to average discharge in the river, whereas Figures 9c and 9d show the effect of reach length into $rRMSE_L$. As with height, slope, and to a certain extent width, longer reaches lead to lower discharge errors (Figures 9c and 9d), with most of the benefits from using longer reaches being achieved once reaches are approximately 15 km in length for the Sacramento River, and 10 km in length for the Po River.

For both rivers, most of the discharge errors due to direct SWOT observations amount to less than 11% of the river discharge. The exceptions occur for the Po River during the highest discharge event, which can be traced back to underestimation of river width during this event. Errors due to direct SWOT observations led to similar discharge errors under the arbitrary 10 km reaches and sinuosity methods for the Sacramento
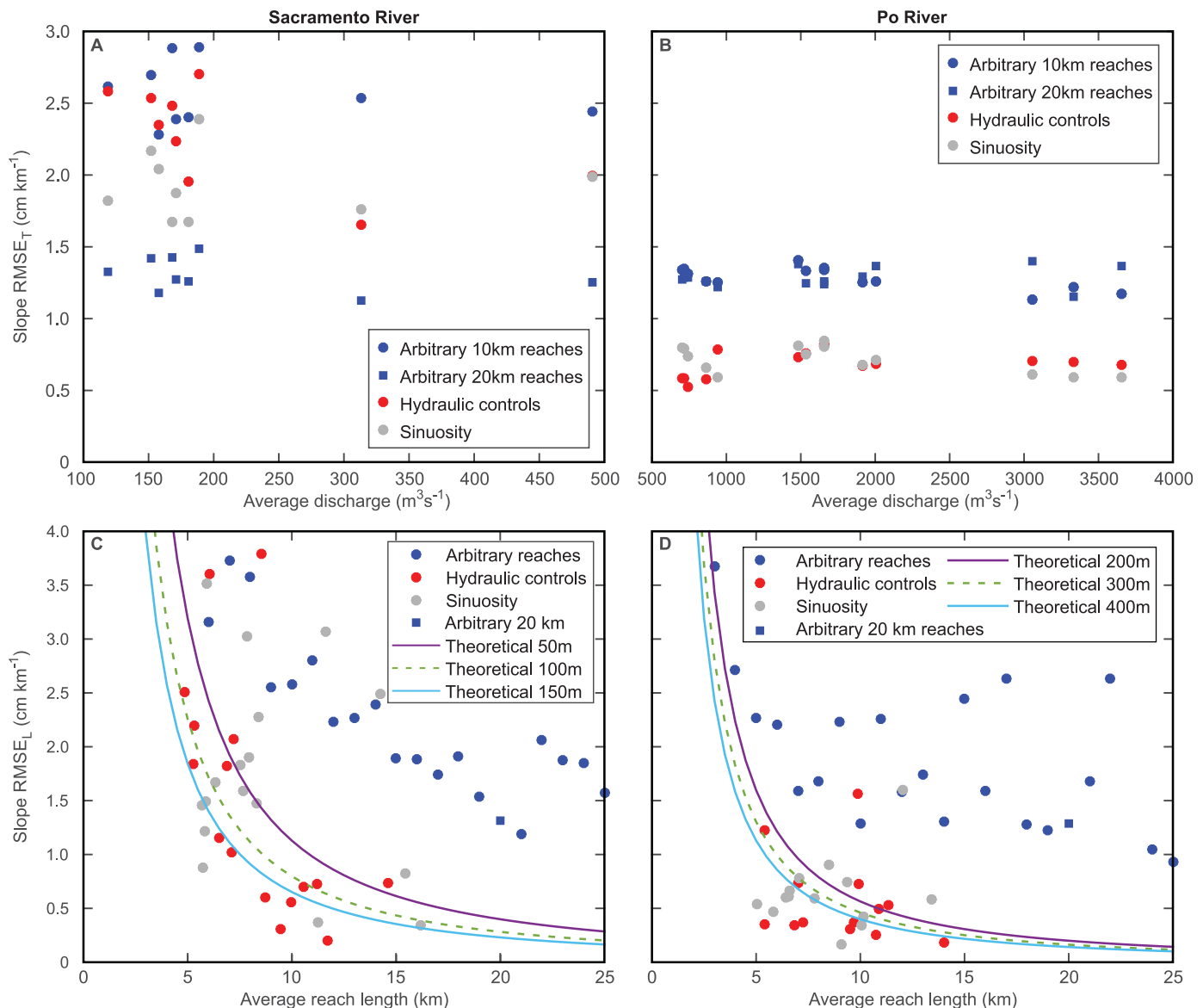
Figure 8. (a) Reach-averaged slope *RMSE* computed for all reaches with length greater than 3 km for each one of the nine overpasses at the Sacramento River versus the average discharge during the overpass. (b) Reach-averaged slope *RMSE* computed for all reaches with length greater than 3 km for each one of the 14 overpasses at the Po River versus the average discharge during the overpass. (c) Time-averaged *RMSE* of reach-averaged slope at the Sacramento River versus reach length. (d) Time-averaged *RMSE* of reach-averaged slope at the Po River versus reach length. Theoretical curves as derived in the SWOT mission performance and error budget document (Esteban-Fernandez, 2013) in the absence of layover errors.

River; whereas the HC outperformed discharge estimates from the 10 km arbitrary reaches during eight out of the nine examined synthetic overpasses despite the shorter HC average reach length. For the Po River, with the exception of the three lowest events, HC and sinuosity reaches led to discharge estimates with error characteristics equal or better than those obtained with 10 and 20 km arbitrary reaches. This is encouraging as it shows that "smart" reach definition strategies could allow the use of shorter reach lengths while keeping errors comparable to arbitrary reaches with longer lengths.

For the Sacramento River, discharge errors due to SWOT measurement uncertainty were lower and more predictable for arbitrary 20 km reaches than they were for HC and Sinuosity reaches. The longer reach lengths were particularly effective in reducing the random component of the slope errors for the Sacramento River, which led to the observed decrease in discharge overpass-based reach-averaged relative $RMSE_T$. This was not the case with the Po River, which is considerably wider than the examined segment of
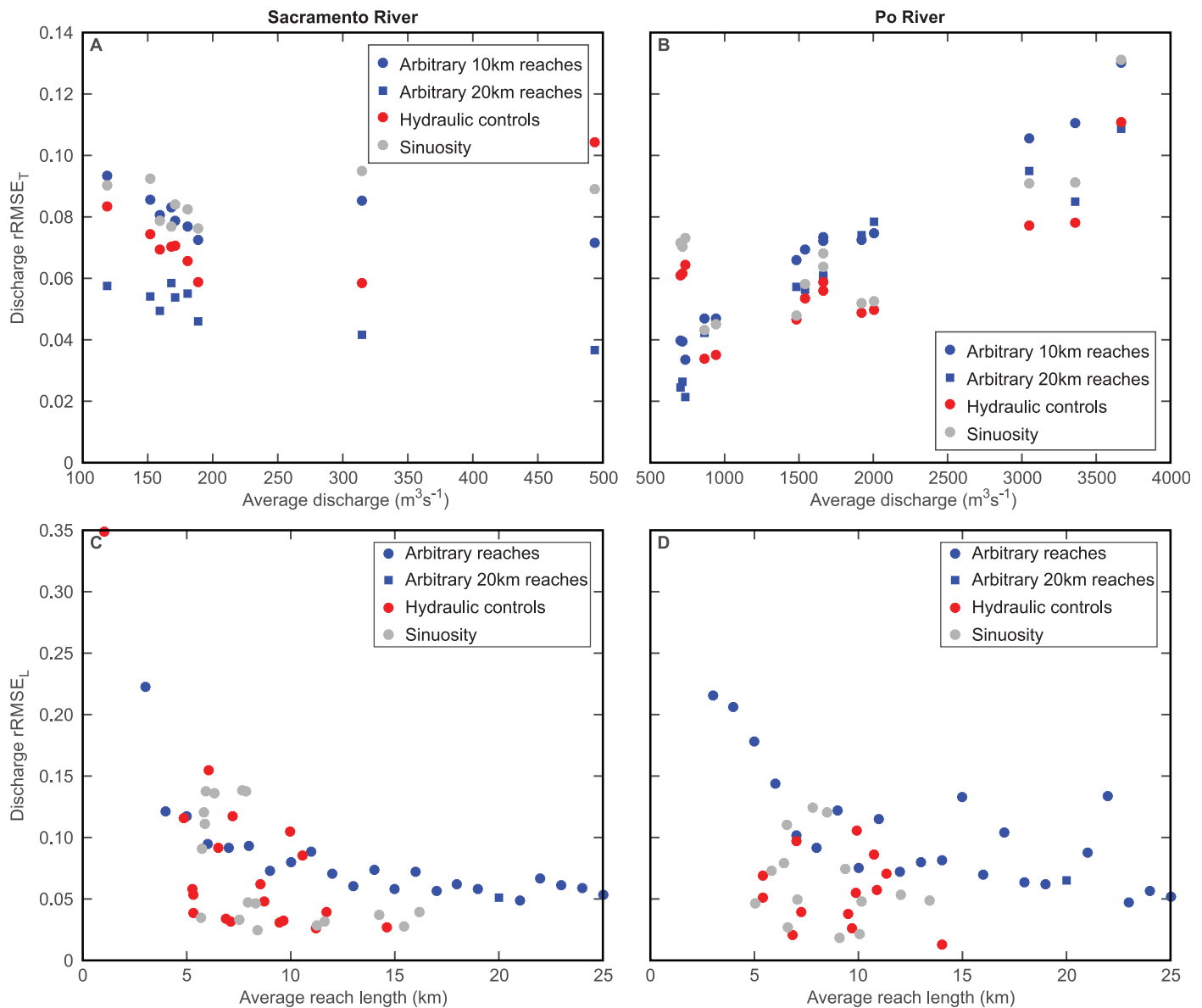
Figure 9. (a) Reach-averaged discharge *rRMSE* computed for all reaches with length greater than 3 km for each one of the nine overpasses at the Sacramento River versus the average discharge during the overpass. (b) Reach-averaged discharge *rRMSE* computed for all reaches with length greater than 3 km for each one of the 14 overpasses at the Po River versus the average discharge during the overpass. (c) Time-averaged *rRMSE* of reach-averaged discharge at the Sacramento River versus reach length. (d) Time-averaged *rRMSE* of reach-averaged discharge at the Po River versus reach length.

the Sacramento River and allows for more averaging across the river width, thus requiring less averaging along the river length to mitigate measurement noise.

Overpass-based reach-averaged relative $RMSE_T$ ($rRMSE_T$) showed opposite behaviors for the Sacramento and the Po Rivers (Figures 9a and 9b). While $rRMSE_T$ initially decreased with increasing discharge for the Sacramento River, it increases for the Po River. Increased errors observed in the Po River are driven by increases in width and cross-sectional area errors with increasing discharge. Nonetheless, it may be possible to address increased area errors during overbank flow by reconstructing river bathymetry using multiple overpasses stacked according to water surface elevation instead of using only heights and widths from the reference and the current overpasses to calculate the areal change ($\delta A_{i,o}$) in equation (10).

As expected, discharge $rRMSE_L$ decreased with increasing reach length (Figures 9c and 9d). Comparing the time-averaged discharge errors for individual reaches produced by the sinuosity and HC methods with

*rRMSE*_L from arbitrary reaches of compatible sizes, we see that most of the smart reaches had smaller errors than their arbitrary counterparts. The smaller discharge errors can be traced back to better reach-averaged heights and slopes produced by the enhanced water surface smoothing technique designed for HC and sinuosity.

Our evaluation of discharge errors only accounts for uncertainties associated with SWOT observations. As stated by Yoon et al. (2016), a larger component of the discharge errors are associated with the estimation of the roughness coefficient ($\tilde{n}_{i,j}$) and the unobservable fraction of the cross-sectional area, i.e., $A_{i,0}$ in equations (10) and (13). Therefore, in addition to allowing better water surface smoothing that preserves more of the river hydraulic properties, which leads to better slope calculation, there could be further benefits to discharge inversion from using smart reach definition strategies such as changes in sinuosity or the identification of the location of hydraulic controls. Ultimately, a comprehensive investigation of the impacts of reach definition strategies into the efficacy of discharge algorithms including more rivers of different sizes, slope, planforms, and orientations with respect to SWOT swaths combined with the multiple state-of-the-art discharge inversion algorithms should support the selection of the river segmentation strategy, or strategies, used throughout the SWOT mission.

4. Conclusion

The choice of river segmentation techniques used to define reaches during the upcoming SWOT mission will affect the quality of anticipated reach-averaged products. This work evaluates three automated river segmentation methods by creating a simulated time series of SWOT overpasses with realistic error characteristics covering fractions of the Sacramento and the Po Rivers. By comparing the performance of two reach definition techniques based on the identification of hydraulic controls and on river sinuosity with products generated by arbitrary reaches of comparable length, we show the potential advantages of employing reach definition methods based on detectable hydraulic properties of the river.

The sinuosity and HC methods applied to the Sacramento and Po Rivers produce average reach lengths smaller than the standard 10 km arbitrary reach length common to other SWOT publications. Nevertheless, the HC and sinuosity methods consistently result in better reach-averaged slope estimates while producing reach-averaged water surface heights and widths with errors that are smaller or comparable to those computed with arbitrary 10 km reaches. More importantly, this work shows that when the estimated reach-averaged height, width, slope, and cross-sectional area errors are propagated to discharge, the HC method often leads to smaller discharge errors than arbitrary 10 km reaches, whereas the sinuosity method, despite its shorter reach lengths, led to discharge errors that were comparable to the arbitrary 10 km reaches. Moreover, in the case of the Po River, both sinuosity and HC methods outperformed the arbitrary 20 km reaches in 9 out of the 14 evaluated overpasses. Such encouraging results indicate that organizing remotely sensed observations of rivers into reaches that attempt to preserve the hydraulic properties of the rivers will likely lead to reduced observational uncertainty, better discharge estimation, and to products that are more meaningful and useful to hydraulic modelers and to the hydrological community. More specifically to SWOT, the present work shows that it is feasible to apply the sinuosity method for the initial definition of SWOT reaches using river centerlines derived from existing Landsat imagery, with posterior use of the HC method for the identification of unlisted hydraulic structures, refinement, and reevaluation of reaches once SWOT data becomes available.

References

Allen, G. H., & Pavelsky, T. M. (2015a). *Characterizing worldwide patterns of fluvial geomorphology and hydrology with the global river widths from landsat (grwl) database.* Paper presented at AGU Fall Meeting, San Francisco, CA, 14–18 December.

Allen, G. H., & Pavelsky, T. M. (2015b). Patterns of river width and surface area revealed by the satellite-derived North American river width data set. *Geophysical Research Letters, 42*, 395–402. https://doi.org/10.1002/2014GL062764

Alsdorf, D. E., & Lettenmaier, D. P. (2003). Tracking fresh water from space. *Science, 301*(5639), 1491–1494. https://doi.org/10.1126/science.1089802

Alsdorf, D. E., Rodríguez, E., & Lettenmaier, D. P. (2007). Measuring surface water from space. *Reviews of Geophysics, 45*, RG2002. https://doi.org/10.1029/2006RG000197

Altenau, E. H., Pavelsky, T. M., Moller, D., Lion, C., Pitcher, L. H., Allen, G. H., . . . Smith, L. C. (2017). Airswot measurements of river water surface elevation and slope: Tanana River, AK. *Geophysical Research Letters, 44*, 181–189. https://doi.org/10.1002/2016GL071577

Andreadis, K. M., Clark, E. A., Lettenmaier, D. P., & Alsdorf, D. E. (2007). Prospects for river discharge and depth estimation through assimilation of swath-altimetry into a raster-based hydrodynamics model. *Geophysical Research Letters*, *34*, L10403. https://doi.org/10.1029/2007GL029721

Biancamaria, S., Hossain, F., & Lettenmaier, D. P. (2011). Forecasting transboundary river water elevations from space. *Geophysical Research Letters*, *38*, L11401. https://doi.org/10.1029/2011GL047290

Biancamaria, S., Lettenmaier, D. P., & Pavelsky, T. M. (2015). The SWOT mission and its capabilities for land hydrology. *Surveys in Geophysics*, *37*, 307–337. https://doi.org/10.1007/s10712-015-9346-y

Birkett, C. M., Mertes, L. A. K., Dunne, T., Costa, M. H., & Jasinski, M. J. (2002). Surface water dynamics in the amazon basin: Application of satellite radar altimetry. *Journal of Geophysical Research*, *107*(D20), 8059. https://doi.org/10.1029/2001JD000609

Bjerklie, D. M. (2007). Estimating the bankfull velocity and discharge for rivers using remotely sensed river morphology information. *Journal of Hydrology*, *341*(3–4), 144–155. https://doi.org/10.1016/j.jhydrol.2007.04.011

Bjerklie, D. M., Dingman, S. L., Vorosmarty, C. J., Bolster, C. H., & Congalton, R. G. (2003). Evaluating the potential for measuring river discharge from space. *Journal of Hydrology*, *278*(1–4), 17–38. https://doi.org/10.1016/S0022-1694(03)00129-X

Bjerklie, D. M., Moller, D., Smith, L. C., & Dingman, S. L. (2005). Estimating discharge in rivers using remotely sensed hydraulic information. *Journal of Hydrology*, *309*(1–4), 191–209. https://doi.org/10.1016/j.jhydrol.2004.11.022

Brenden, T. O., Wang, L., Seelbach, P. W., Clark, R. D., Jr., Wiley, M. J., & Sparks-Jackson, B. L. (2008). A spatially constrained clustering program for river valley segment delineation from GIS digital river networks. *Environmental Modelling & Software*, *23*(5), 638–649. https://doi.org/10.1016/j.envsoft.2007.09.004

Castellarin, A., Di Baldassarre, G., & Brath, A. (2011a). Floodplain management strategies for flood attenuation in the river Po. *River Research and Applications*, *27*(8), 1037–1047. https://doi.org/10.1002/rra.1405

Castellarin, A., Domeneghetti, A., & Brath, A. (2011b). Identifying robust large-scale flood risk mitigation strategies: A quasi-2d hydraulic model as a tool for the Po River. *Physics and Chemistry of the Earth, Parts A/B/C*, *36*(7–8), 299–308. https://doi.org/10.1016/j.pce.2011.02.008

Chin, D. A. (2006). *Water-resources engineering* (2nd ed.). Upper Saddle River, NJ: Pearson Prentice Hall.

Chow, V. (1959). *Open-channel hydraulics*. New York, NY: Mc Graw-Hill.

Dingman, S. L. (2007). Analytical derivation of at-a-station hydraulic–geometry relations. *Journal of Hydrology*, *334*(1–2), 17–27. https://doi.org/10.1016/j.jhydrol.2006.09.021

Dingman, S. L., & Bjerklie, D. M. (2006). Estimation of river discharge. In *Encyclopedia of hydrological sciences* (Vol. 5, Chapter 61, 19 pp.). Hoboken, NJ: John Wiley & Sons. https://doi.org/10.1002/0470848944.hsa069

Domeneghetti, A., Tarpanelli, A., Brocca, L., Barbetta, S., Moramarco, T., Castellarin, A., & Brath, A. (2014). The use of remote sensing-derived water surface data for hydraulic model calibration. *Remote Sensing of Environment*, *149*, 130–141. https://doi.org/10.1016/j.rse.2014.04.007

Durand, M., Andreadis, K. M., Alsdorf, D. E., Lettenmaier, D. P., Moller, D., & Wilson, M. (2008). Estimation of bathymetric depth and slope from data assimilation of swath altimetry into a hydrodynamic model. *Geophysical Research Letters*, *35*, L20401. https://doi.org/10.1029/2008GL034150

Durand, M., Fu, L. L., Lettenmaier, D. P., Alsdorf, D., Rodríguez, E., & Esteban-Fernandez, D. (2010a). The surface water and ocean topography mission: Observing terrestrial surface water and oceanic submesoscale eddies. *Proceedings of the IEEE*, *98*(5), 766–779. https://doi.org/10.1109/jproc.2010.2043031

Durand, M., Gleason, C. J., Garambois, P. A., Bjerklie, D., Smith, L. C., Roux, H., . . . Vilmin, L. (2016). An intercomparison of remote sensing river discharge estimation algorithms from measurements of river height, width, and slope. *Water Resources Research*, *52*, 4527–4549. https://doi.org/10.1002/2015WR018434

Durand, M., Neal, J., Rodríguez, E., Andreadis, K. M., Smith, L. C., & Yoon, Y. (2014). Estimating reach-averaged discharge for the River Severn from measurements of river water surface elevation and slope. *Journal of Hydrology*, *511*, 92–104. https://doi.org/10.1016/j.jhydrol.2013.12.050

Durand, M., Rodríguez, E., Alsdorf, D. E., & Trigg, M. (2010b). Estimating river depth from remote sensing swath interferometry measurements of river height, slope, and width. *IEEE Journal of Selected Topics in Applied Earth Observations and Remote Sensing*, *3*(1), 20–31. https://doi.org/10.1109/jstars.2009.2033453

Esteban-Fernandez, D. (2013). *SWOT mission performance and error budget* (Rep. JPL D-79084 Revision A). Pasadena, CA: Jet Propulsion Laboratory. Retrieved from http://swot.jpl.nasa.gov/files/SWOT_D-79084_v5h6_SDT.pdf

Farr, T. G., Rosen, P. A., Caro, E., Crippen, R., Duren, R., Hensley, S., . . . Alsdorf, D. (2007). The shuttle radar topography mission. *Reviews of Geophysics*, *45*, RG2004. https://doi.org/10.1029/2005RG000183

Fjørtoft, R., Gaudin, J.-M., Pourthie, N., Lalaurie, J.-C., Mallet, A., Nouvel, J.-F., . . . Daniel, S. (2014). Karin on SWOT: Characteristics of near-nadir Ka-band interferometric SAR imagery. *IEEE Transactions on Geoscience and Remote Sensing*, *52*(4), 2172–2185. https://doi.org/10.1109/tgrs.2013.2258402

Garambois, P. A., Calmant, S., Roux, H., Paris, A., Monnier, J., Finaud-Guyot, P., Samine Montazem, A., & Santos da Silva, J. (2017). Hydraulic visibility: Using satellite altimetry to parameterize a hydraulic model of an ungauged reach of a braided river. *Hydrological Processes*, *31*(4), 756–767. https://doi.org/10.1002/hyp.11033

Garambois, P. A., & Monnier, J. (2015). Inference of effective river properties from remotely sensed observations of water surface. *Advances in Water Resources*, *79*, 103–120. https://doi.org/10.1016/j.advwatres.2015.02.007

Gleason, C. J., & Hamdan, A. N. (2015). Crossing the (watershed) divide: Satellite data and the changing politics of international river basins. *The Geographical Journal*, *183*, 2–15. https://doi.org/10.1111/geoj.12155

Gleason, C. J., & Smith, L. C. (2014). Toward global mapping of river discharge using satellite images and at-many-stations hydraulic geometry. *Proceedings of the National Academy of Sciences of the United States of America*, *111*(13), 4788–4791. https://doi.org/10.1073/pnas.1317606111

Gleason, C. J., Smith, L. C., & Lee, J. (2014). Retrieval of river discharge solely from satellite imagery and at-many-stations hydraulic geometry: Sensitivity to river form and optimization parameters. *Water Resources Research*, *50*, 9604–9619. https://doi.org/10.1002/2014WR016109

Hossain, F., Siddique-E-Akbor, A. H., Mazumder, L. C., ShahNewaz, S. M., Biancamaria, S., Lee, H., & Shum, C. K. (2014). Proof of concept of an altimeter-based river forecasting system for transboundary flow inside Bangladesh. *IEEE Journal of Selected Topics in Applied Earth Observations and Remote Sensing*, *7*(2), 587–601. https://doi.org/10.1109/jstars.2013.2283402

Ikeda, S. (1984). Prediction of alternate bar wavelength and height. *Journal of Hydraulic Engineering*, *110*(4), 371–386. https://doi.org/10.1061/(ASCE)0733-9429(1984)110:4(371)

Ikeda, S., Parker, G., & Sawai, K. (1981). Bend theory of river meanders. Part 1. Linear development. *Journal of Fluid Mechanics*, *112*, 363–377. https://doi.org/10.1017/S0022112081000451

Kiel, B. A. (2015). *Measurements of U.S. rivers clarify river-shaping factors and interaction with groundwater* (PhD dissertation, 151 pp.). Austin: University of Texas. https://doi.org/10.15781/T2D062

Kondolf, G. M., & Batalla, R. J. (2005). Chapter 11 hydrological effects of dams and water diversions on rivers of Mediterranean-climate regions: Examples from California. In G. Celso & J. B. Ramon (Eds.), *Catchment dynamics and river processes: Mediterranean and other climate regions* (pp. 197–211). New York, NY: Elsevier. https://doi.org/10.1016/S0928-2025(05)80017-3

LeFavour, G., & Alsdorf, D. (2005). Water slope and discharge in the Amazon River estimated using the shuttle radar topography mission digital elevation model. *Geophysical Research Letters*, *32*, L17404. https://doi.org/10.1029/2005GL023836

Leopold, L. B., & Maddock, T. (1953). The hydraulic geometry of stream channels and some physiographic implications. *Geological Survey Professional Paper*, *252*, 64.

Leopold, L. B., & Wolman, M. G. (1957). *River channel patterns: Braided, meandering, and straight*. Washington, DC: U.S. Government Printing Office.

Leopold, L. B., & Wolman, M. G. (1960). River meanders. *Geological Society of America Bulletin*, *71*(6), 769–793. https://doi.org/10.1130/0016-7606(1960)71[769:RM]2.0.CO;2

Martínez-Fernández, V., Solana-Gutiérrez, J., González del Tánago, M., & García de Jalón, D. (2016). Automatic procedures for river reach delineation: Univariate and multivariate approaches in a fluvial context. *Geomorphology*, *253*, 38–47. https://doi.org/10.1016/j.geomorph.2015.09.029

Minear, J. T. (2010). *The downtream geomorphic effects of dams: A comprehensive and comparative approach* (PhD dissertation, 2017 pp.). University of California, Berkley. Retrieved from http://escholarship.org/uc/item/1f8612f9

Montanari, A., Ceola, S., Baratti, E., Domeneghetti, A., & Brath, A. (2016). Po river basin. In V. P. Singh (Ed.), *Handbook of applied hydrology* (p. 4). New York, NY: McGraw Hill Education.

Munier, S., Polebistki, A., Brown, C., Belaud, G., & Lettenmaier, D. P. (2015). SWOT data assimilation for operational reservoir management on the upper Niger River basin. *Water Resources Research*, *51*(1), 554–575. https://doi.org/10.1002/2014WR016157

Odgaard, A. J. (1986). Meander flow model. I: Development. *Journal of Hydraulic Engineering*, *112*(12), 1117–1135. https://doi.org/10.1061/(ASCE)0733-9429(1986)112:12(1117)

Odgaard, A. J., & Abad, J. D. (2008). River meandering and channel stability. In *Sedimentation engineering: Processes, measurements, modeling, and practice. American society of civil engineers, manuals and reports on engineering practice*, edited (pp. 439–460). Reston, VA: American Society of Civil Engineers. https://doi.org/10.1061/9780784408148.ch08

O'Loughlin, F., Trigg, M. A., Schumann, G. J. P., & Bates, P. D. (2013). Hydraulic characterization of the middle reach of the Congo River. *Water Resources Research*, *49*, 5059–5070. https://doi.org/10.1002/wrcr.20398

Parker, C., Clifford, N. J., & Thorne, C. R. (2012). Automatic delineation of functional river reach boundaries for river research and applications. *River Research and Applications*, *28*(10), 1708–1725. https://doi.org/10.1002/rra.1568

Parker, G., Diplas, P., & Akiyama, J. (1983). Meander bends of high amplitude. *Journal of Hydraulic Engineering*, *109*(10), 1323–1337. https://doi.org/10.1061/(ASCE)0733-9429(1983)109:10(1323)

Pavelsky, T. M., Durand, M., Andreadis, K. M., Beighley, R. E., Paiva, R. C. D., Allen, G. H., & Miller, Z. F. (2014). Assessing the potential global extent of SWOT river discharge observations. *Journal of Hydrology*, *519*, 1516–1525. https://doi.org/10.1016/j.jhydrol.2014.08.044

Rodríguez, E. (2015). *Surface Water and Ocean Topography Mission (SWOT), science requirements document* (Rep. JPL document D-61923). Pasadena, CA: Jet Propulsion Laboratory. Retrieved from https://swot.jpl.nasa.gov/files/swot/SRD_021215.pdf

Rogers, W. (2014). *Central valley floodplain evaluation and delineation, subtask 5, combined Sacramento River system model* (Technical Memorandum 841). Sacramento: California Department of Water Resources.

Rosgen, D. L. (1994). A classification of natural rivers. *Catena*, *22*(3), 169–199. https://doi.org/10.1016/0341-8162(94)90001-9

Roux, H., & Dartus, D. (2005). Parameter identification using optimization techniques in open-channel inverse problems. *Journal of Hydraulic Research*, *43*(3), 311–320. https://doi.org/10.1080/00221680509500125

Schumann, G., Di Baldassarre, G., Alsdorf, D., & Bates, P. D. (2010). Near real-time flood wave approximation on large rivers from space: Application to the river Po, Italy. *Water Resources Research*, *46*, W05601. https://doi.org/10.1029/2008WR007672

Smith, A., Sampson, C., & Bates, P. (2015). Regional flood frequency analysis at the global scale. *Water Resources Research*, *51*, 539–553. https://doi.org/10.1002/2014WR015814

Sneddon, C., & Fox, C. (2012). Water, geopolitics, and economic development in the conceptualization of a region. *Eurasian Geography and Economics*, *53*(1), 143–160. https://doi.org/10.2747/1539-7216.53.1.143

Solander, K. C., Reager, J. T., & Famiglietti, J. S. (2016). How well will the surface water and ocean topography (SWOT) mission observe global reservoirs? *Water Resources Research*, *52*, 2123–2140. https://doi.org/10.1002/2015WR017952

Wolf, A. T., Natharius, J. A., Danielson, J. J., Ward, B. S., & Pender, J. K. (1999). International river basins of the world. *International Journal of Water Resources Development*, *15*(4), 387–427. https://doi.org/10.1080/07900629948682

Yoon, Y., Durand, M., Merry, C. J., Clark, E. A., Andreadis, K. M., & Alsdorf, D. E. (2012). Estimating river bathymetry from data assimilation of synthetic SWOT measurements. *Journal of Hydrology*, *464*, 363–375. https://doi.org/10.1016/j.jhydrol.2012.07.028

Yoon, Y., Garambois, P.-A., Paiva, R. C. D., Durand, M., Roux, H., & Beighley, E. (2016). Improved error estimates of a discharge algorithm for remotely sensed river measurements: Test cases on Sacramento and Garonne Rivers. *Water Resources Research*, *52*, 278–294. https://doi.org/10.1002/2015WR017319